University of Padova

Department of Information Engineering

Master Thesis in Telecommunication Engineering

Polarization Sensitive Optical Coherence Tomography: optimization and application to zebrafish imaging

Student

Nicola Volpato

Advisor

Prof. Luca Palmieri

Academic Year 2015/2016

Ai miei genitori e mio fratello Davide, per tutto quello che hanno fatto per me in questi anni di studio credendo in me e supportando ogni mia scelta.

A Filippo, il vero amico che sa sostenermi anche nel silenzio.

Ad Arianna, Barbara, Chiara e Denise, che con la loro amicizia hanno saputo strapparmi un sorriso anche nella stanchezza.

A tutto il gruppo educatori dell'Azione Cattolica e don Michele, per le condivisioni, le avventure e le sfide superate assieme in questi ultimi anni.

Ai miei nonni che, anche se non sono più qui, sono sicuramente orgogliosi di me in questo momento così importante.

Al professor Palmieri, per l'attenzione mostrata verso questo progetto e il suo costante aiuto.

A tutti, un sincero grazie.

> [...] Uno dei due che avevano udito le parole di Giovanni e lo avevano seguito, era Andrea, fratello di Simon Pietro. Egli incontrò per primo suo fratello Simone e gli disse: «Abbiamo trovato il Messia» – che si traduce Cristo – e lo condusse da Gesù. Fissando lo sguardo su di lui, Gesù disse: «Tu sei Simone, il figlio di Giovanni; sarai chiamato Cefa» – che significa Pietro.
>
> *Gv 1, 40-42*

Abstract

Optical Coherence Tomography is a transversal imaging technique that is used to obtain topographical images of micrometer structures and biological samples through the analysis of their retroreflected light. Polarization-Sensitive OCT is its functional extension and it takes advantage of the changes in polarization as light travels through tissues to provide additional information about the sample under examination and evaluate the birefringence of the material. PS-OCT is used in clinical applications less frequently than traditional OCT because of the high complexity of actual systems and the need for sophisticated synchronization controls. In this thesis we present a PS-OCT entirely built with fiber optic components that is simple and robust, based on tunable source technology. We tested the functionality of the system first on an adhesive tape and then on a biological sample, a Zebrafish specimen.

Contents

List of Figures

List of Tables

Chapter 1

Introduction

Optical coherence tomography (OCT) is a transversal imaging technique that is used to obtain high resolution tomographical images of micrometer structures and biological systems. OCT is similar to other clinical imaging techniques like echography, which uses ultrasound instead of light, and differs from them in axial and transversal resolution. This imaging technique is suitable to diagnostic medical applications because it has multiple advantages such as non invasiveness and the ability to take measurements without actual physical contact with the sample under investigation [1], as images are obtained by hitting the sample with light and measuring the intensity and the properties of the reflected light. The depth of inspection with OCT is mainly limited by scattering and absorption of the tissue under investigation but it is possible to obtain images with a depth of 2-3 mm in almost all cases. OCT can be a viable alternative to impossible or risky biopsies, and because of its peculiarities it is often used in the diagnosis of cardiovascular and dermatological diseases, where less invasive and faster techniques are required. For example, nowadays ophthalmic OCT is very important in the analysis of ocular structures and their possible diseases, thanks to its micrometer resolution with a maximum depth of a few millimetres [2]. This technique has had a remarkable development because light has a limited absorption in human tissues and with the use of catheters and endoscopes it is possible to reach tissues inside the human body in order to inspect and monitor, for example, cancer cells, cardiovascular occlusions, and the cartilage of joints, tendons

and ligaments [1].

Traditional OCT is used to obtain intensity images and it does not allow to recognize different types of tissues. Polarization-Sensitive OCT (PS-OCT) is its functional extension and it takes advantage of the changes in polarization as light goes through tissues to provide additional information about the sample under examination: birefringent tissues are known to change phase delays between different polarizations. Tissues such as muscles, tendons, nerves, bones, teeth exhibit birefringence and the alteration of the birefringence of tissues is often due to disease progression. An example could be the loss of birefringence of retinal nerves observed during the initial phase of glaucoma. PS-OCT has different applications like the imaging of skin, assessment of damage and thermal burns, dental imaging and the characterization of atherosclerotic plaques [3].

Since their introduction in 1992, PS-OCT technologies have had a remarkable development and we can divide them in two different categories based on the knowledge of the exact state of polarization of the light used to illuminate the sample. When the state of the incident light is known a priori, birefringence data for a given tissue is obtained from a polarization-sensitive detector and the ratio between the intensity of the two (orthogonal) polarization channels detected. In contrast to this first category, which is suitable to be implemented in free space, in systems based on fiber optic components, where input and output polarization states are not precisely known due to possible modifications of their optical properties during the image acquisition, the sample is hit with light in two or more different states of polarization (SOP). Different PS-OCT systems of this type have been developed in the last few years, where different SOPs are sequentially or simultaneously acquired [4, 5]. Passive polarization multiplexing has also been recently demonstrated, through the coding of the states of polarization at different depths with a single A-scan [6, 7] and without the use of active synchronization components.

In contrast with the commercialization of OCT in medical applications such as ocular and cardiovascular imaging, free space misalignments and the need for sophisticated synchronization controls have limited the clinical diffusion of PS-OCT which is used less frequently because of the high complexity

of actual systems.

In this thesis we present two different OCT systems based on fiber optics components and the use of a tunable source: both of them are polarization sensitive but the second one is particularly suitable for the measurement of the birefringence of a sample under test. Firstly, in Chapter 2 we present the underlying physical principles for the instrumentation we used. In Chapter 3 and 4 we present respectively the OCT tecnique and the two setups we tested and finally in Chapter 5 we report the results of the tests carried out on different biological and non-biological samples.

Chapter 2

Physical principles

In this chapter we present the physical principles of electromagnetism that are the basis of OCT technologies. Firstly we give the definition of coherence, which is necessary for the analysis of interference and beat between waves. Then we will review some important notions from electromagnetic theory and describe the models used to evaluate birefringence and polarization.

2.1 Coherence

Coherence is a difficult and complex topic, but it is the basis of OCT theory [8]. Coherence could be defined as the degree of correlation between two interfering beams of light. If we observe the light emitted from a natural source, we will see that it is made of indipendently emitted photons that result from the energetic decay of a large number of atoms, each of which emits photons at different frequencies and phases. Their overlay produces a wave front that is irregular and aleatory. This type of radiation is said to be incoherent or partially coherent. When, on the other hand, the dependence of the wave front on time and position in space is known and invariant, we say that the light is coherent.
An example of coherent light is the light emitted from a laser. This type of radiation is monochromatic and its electric field is

$$E(\mathbf{r}, t) = E(\mathbf{r}) \exp[j(2\pi\nu t + \phi)], \tag{2.1}$$

which is deterministic and so is its optic intensity. In the case of incoherent light, the electric field shows aleatory fluctuations and intensity has to be defined as the average over time of its instantaneous value.

A laser emits coherent light that is almost monochromatic. In general light is emitted during the transition of an electron from a high energy state to a lower energy one. The light is not completely monochromatic because atoms in excited state are not static and they continuously collide losing or gaining energy as a result. The frequency of light is directly proportional to its energy (E=hf), so collisions with their subsequent modifications of the energy of single atoms produce variations in frequency of the photons emitted during the decay of the electrons. Another mechanism that produces emissions at different frequencies is the Doppler effect: atoms in exited states are moving in different directions and this affects the frequency of emitted light.

For a precise analysis of coherence and its properties we refer to previous works [9]. Here we use a quantitative approach to coherence and we will consider the emissions from two different atoms. These emissions take place at slightly different times and they show small differences in frequency. They overlap, but not completely. The period of time during which the emissions from two different sources can be considered coherent is defined as coherence time. This interval is always finite but in an optical system, it could be assumed that light is actually coherent and maintains its regularity properties. The distance travelled by the light during this time is defined as radiation coherence length and it is the product of coherence time and speed of light in the system. In the real sources used in OCT systems, light is emitted from many atoms and it maintains an almost constant intensity. So coherence length is affected by the small differences in the frequency and phases of the beam of light. However it is important to note that the sources of light used in OCT systems guarantee a level of coherence that is sufficient for the purposes of this particular application.

2.2 Interferometry

OCT measures the interference between a lightwave and its translated version. This is done using an interferometer, an optical device that divides the input radiation into two beams: one is sent to the sample and one to the reference arm. OCT then exploits the phenomenon of interference to measure spectral properties of the reflected light that cannot be measured directly. As explained in section 4.1.1 the instrument we used for this purpose is based on Michelson's interferometer [8].

As can be seen in Figure 2.1 the light emitted from the source is divided by a beam splitter. Half of the light is sent to the sample under investigation (in this case a mirror) and half to the reference arm, that holds a mobile mirror. Light is reflected by each mirror and recombined at the beam splitter, where the two beams are recombined and the resulting light is collected by a detector.

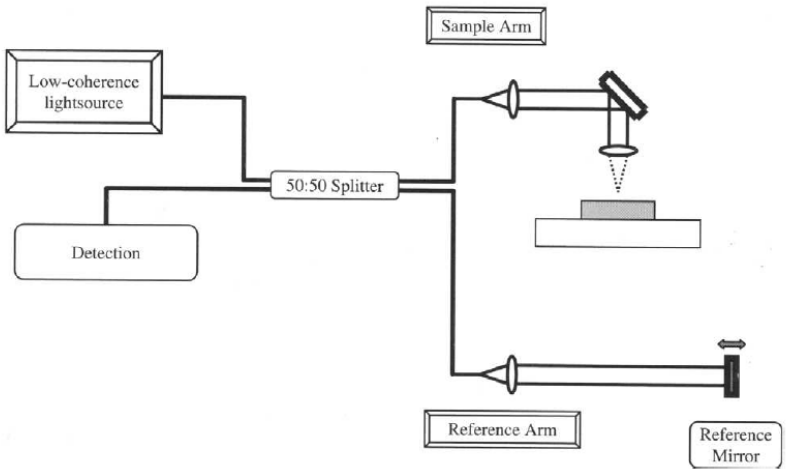

Figure 2.1: Simplified scheme of an interferometer. Image taken from [10].

2.2.1 Interference of a monochromatic wave

When two or more optical waves interfere their sum can be obtained from the principle of superimposition of the effects. The complex amplitudes of the electric fields are added, but the resulting intensity also depends on the

phase displacement of the two waves, the coherence length of the radiations and their frequencies: the result is interference and beat.

In an interferometer the light of the source is divided into two waves E_r and E_s, which are the electric fields of the two arms. These two waves are also monochromatic and have the same frequency and phase. We can describe the dependence of the amplitude E on the phase and the frequency using equation 2.22. Considering the light reflected by the sample and by the mirror in the reference arm, and overlaying them at the beam splitter we obtain another monochromatic radiation given by the sum

$$E_{tot}(\mathbf{r}, t) = E_r(\mathbf{r}, t) + E_s(\mathbf{r}, t), \tag{2.2}$$

where we assume that all the light is reflected back by the sample (a mirror) and the reference arm. Furthermore these two monochromatic waves travel different distances and so their phases are different when they interfere. The interferometer measures the optic intensity of each wave which is proportional to the square of the absolute value of the electric field. So, the intensity of their sum is

$$\begin{aligned} I &\propto \frac{|E_{tot}|^2}{2} \\ &\propto \frac{|E_r|^2}{2} + \frac{|E_s|^2}{2} + Re[E_r^* E_s], \end{aligned} \tag{2.3}$$

and substituting the expressions of the electric field we obtain

$$\begin{aligned} I &\propto \frac{|E_r|^2}{2} + \frac{|E_s|^2}{2} + E_r E_s \cdot Re[\exp(j(\phi_r - \phi_s))] \\ &\propto \frac{|E_r|^2}{2} + \frac{|E_s|^2}{2} + E_r E_s \cos(\phi) \\ &= I_r + I_s + 2\sqrt{I_r I_s}\cos(\phi), \end{aligned} \tag{2.4}$$

where $\phi = \phi_r - \phi_s$.
From this expression, we can see that the total intensity reflected is not simply the sum of the two intensities. It also depends on the phases of the two beams and we can precisely evaluate the phase displacement between the two waves by measuring the intensity of their sum. The last term in the previous equation is the interference term which can be either positive or

negative: when the angle ϕ is 0 or a multiple of $\pm 2\pi$, the two waves are said to be in phase, the cosine has a maximum and so does the total intensity (here we have constructive interference). On the other hand, when ϕ is equal to $(2k+1)\pi$ with $k = \pm 1, \pm 2, ...$, the cosine and the intensity both have a minimum (destructive interference).

2.2.2 Interference of two monochromatic waves

For a qualitative approach to this subject we refer to [10]. Here we will use a quantitative approach and we will consider two waves with electric fields $E_r(\mathbf{r}, t)$ and $E_s(\mathbf{r}, t)$, but with different frequencies ν_r and ν_s and phases $\phi_r = \phi_s = 0$ for simplicity. Unlike the interference between two waves with the same frequency, the interference between two waves with different frequencies generates amplitude modulation, also known as beat. As in equation 2.2 the sum of the two radiations and its optical intensity is

$$\begin{aligned} E_{tot}(\mathbf{r}, t) &= E_r(\mathbf{r}, t) + E_s(\mathbf{r}, t) \\ I(t) &\propto \frac{1}{2}\left[|E_{tot}(t)|^2 = |E_r(t)|^2 + |E_s(t)|^2 + 2Re[E_r^* E_s]\right] \\ &= I_r + I_s + 2\sqrt{I_r I_s}\cos[2\pi(\nu_r - \nu_s)t]. \end{aligned} \tag{2.5}$$

If we choose $I_r = I_s = I_0$ equation 2.5 becomes

$$I = 2I_0[1 + \cos\psi], \tag{2.6}$$

where $\psi = 2\pi(\nu_r - \nu_s)t$. We can see that the total intensity varies with a sinusoidal frequency of $\nu_{beat} = \nu_r - \nu_s$, the beat frequency. Destructive and constructive interferences alternate because of the difference between the two frequencies and we can evaluate two cases:

- $\psi = 0$, the interference is constructive and I has a maximum. In this case we have complete coherence between the two waves;
- $\psi \neq 0$, we have only partial coherence between the two waves.

In Figure 2.2 we can see the envelope at the frequency ν_{beat}. Since a photodetector of area A measures the optical power

$$P(t) = \int_A I(\mathbf{r}, t) dA, \tag{2.7}$$

it detects a signal with frequency equal to the beat frequency ν_{beat}.

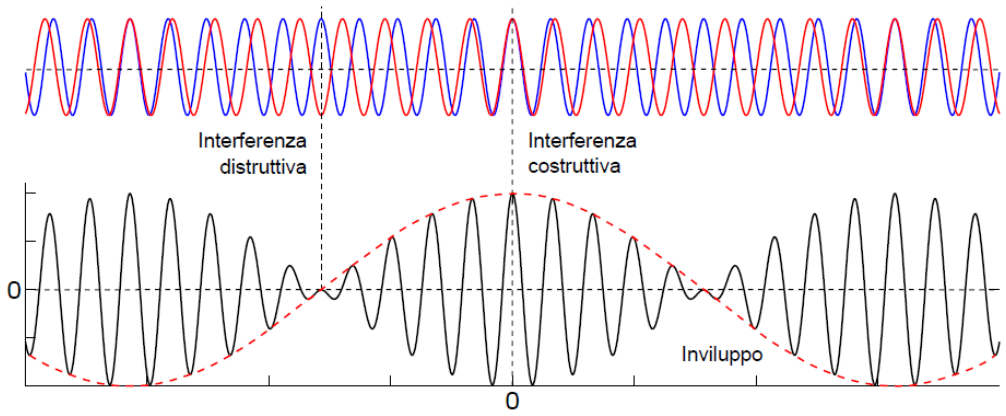

Figure 2.2: Beat between two sinusoids with different frequency. Image taken from [9].

2.2.3 Interference and coherence

Interference can be observed only when the light is coherent. When this assumption is not satisfied, the random fluctuations of ϕ_r and ϕ_s cause a phase shift that can be described by a random variable with uniform distribution in $[0, 2\pi]$ and with mean value equal to π. If we compute the expectation of $\cos(\phi)$ with $\phi \in [0, 2\pi]$ we obtain $E[\cos(\phi)] = 0$. If we now consider equation 2.4 we can see that the interference term disappears. However interference can take place also with broad-spectrum sources, within the length of coherence associated to the wave.

In order to compute the intensity of the retroreflection [8] OCT uses the mutual correlation between two different waves, which is defined, at position $\mathbf{r}$ and time t, as

$$G_{rs} = \left\langle |E_r^* E_s| \right\rangle. \tag{2.8}$$

Its normalized form is

$$g_{rs} = \frac{G_{rs}}{\sqrt{I_r I_s}}. \tag{2.9}$$

Using these relationship equation 2.5 becomes

$$\begin{aligned} I &\propto \frac{1}{2}[\langle |E_r + E_s|^2 \rangle] \\ &\propto \frac{1}{2}\left[\langle |E_r|^2 \rangle + \langle |E_s|^2 \rangle + \langle |E_r^* E_s| \rangle + \langle |E_r E_s^*| \rangle\right] \\ &= I_r + I_s + 2\sqrt{I_r I_s} Re[g_{rs}] \\ &= I_r + I_s + 2\sqrt{I_r I_s}|g_{rs}| \cos(\phi_{rs}), \end{aligned} \tag{2.10}$$

where ϕ_{rs} is the phase associated to g_{rs} which defines the interference. We can easily see that:

- for $g_{rs} = 1$ the two waves are correlated and we obtain equation 2.4;
- for $g_{rs} = 0$ the two waves are uncorrelated and the interference term goes to zero;
- for $0 < |g_{rs}| < 1$ the waves are partially correlated and the optical intensity is sinusoidal.

If we now consider the interference between a wave and its version shifted by the amount τ (the time delay between the two arms of the interferometer) we obtain (from equation 2.10)

$$I = 2I_0[1 + |g(\tau)| \cos(\phi(\tau))], \tag{2.11}$$

assuming $I_r = I_s = I_0$. The interference term depends on the degree of autocorrelation $g(\tau)$ which in turn depends on the coherence time τ_c. If we consider the normalized version of the intensity we can define visibility as

$$V = \frac{I_{max} - I_{min}}{I_{max} + I_{min}} = \frac{2\sqrt{I_r I_s}}{I_r - I_s}|g_{rs}|, \tag{2.12}$$

which becomes

$$V = |g_{rs}|, \tag{2.13}$$

if $I_r = I_s = I_0$.

In the case of an OCT source, where the wave emitted is only partially coherent, the associated electric field is

$$E(\mathbf{r}, t) = E_a(t) \exp(j2\pi\nu t), \tag{2.14}$$

where $E_a(t)$ is a random function used to simulate the behaviour of a non-coherent wave. The autocorrelation between the wave and its shifted version is

$$\begin{aligned} G(\tau) &= G_a(\tau)\exp(j2\pi\nu\tau), \\ g(\tau) &= |g_a(\tau)|\exp[j(2\pi\nu\tau + \phi_a(\tau))], \end{aligned} \tag{2.15}$$

where $G_a(\tau) = \left\langle E_a^*(t)E_a(t+\tau)\right\rangle$ and $g_a(\tau) = |g_a(\tau)|\exp[j\phi_a(\tau)]$. Substituting $g(\tau)$ in equation 2.11 we obtain

$$I = 2I_0[1 + |g_a(\tau)|\cos(2\pi\nu\tau + \phi_a(\tau))], \tag{2.16}$$

which is the correlation between the delay τ and the intensity of the interferogram. The visibility now changes with τ and has its maximum when $\tau = 0$ and is 0 when $\tau > \tau_c$. Therefore there is interference only when the delay between the two waves is less than the coherence time and in particular if and only if $\Delta l < l_c$ (l_c is the coherence length).

2.3 Gaussian beams

Optical applications as OCT need a more detailed description of the radiation than what can be obtained by simply approximating it with geometrical optics.
The Gaussian beam is an approximated solution of Helmholtz's equation: the power is mainly concentrated in a cylinder around the propagation axis and the distribution of the intensity is described, in each transverse plane, by a Gaussian function centred on the axis of propagation. This function has its minimum width when it reaches the beam waist and grows as we move away from it in both directions, with a subsequent divergence of the beam. It can be demonstrated [9] that the optical intensity of the Gaussian beam is a function of its axial and radial position and that it reaches its maximum value at the beam waist, where the radius of the beam has a minimum.

In Figure 2.3 it can be seen how an optical beam propagates through a lens. The incident light maintains its Gaussian properties, but the position of the beam waist and its divergence after the lens are now dependent on its focal length *f*. The width of incident beam is the same as that of the beam

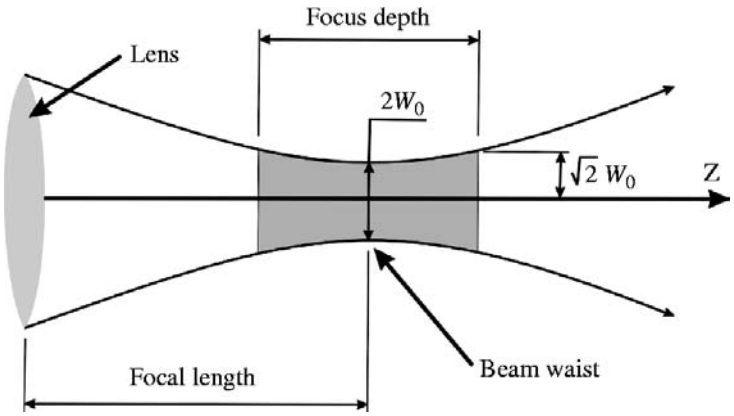

Figure 2.3: Transmission of a Gaussian beam through a lens. Image taken from [11].

at the output interface of the lens and its parameters depend on the input ones [9].
As we can see in Figure 2.3 the focus depth is defined as double the distance at which the intensity is half of its maximum value I_0 and here the radius of the beam reaches the value of $\sqrt{2}W_0$ [12]. From the equation of the radius

$$W(z) = W_0\sqrt{1 + \left(\frac{z}{z_0}\right)^2}, \tag{2.17}$$

we can calculate the focus depth as

$$2z_0 = \frac{2\pi W_0^2}{\lambda}, \tag{2.18}$$

where z_0 is called Rayleigh's distance and W_0 is the radius of the beam at the "beam waist". For $z \gg z_0$ equation 2.17 becomes

$$W(z) \simeq \frac{W_0}{z_0} z = \theta_0 z. \tag{2.19}$$

Namely, at a great distance, the beam diverges with a semi-angle θ_0 and as we reduce the beam waist W_0, the divergence increases and as a consequence the focus depth decreases: this represents an important compromise for the performances of OCT systems in terms of transversal resolution.

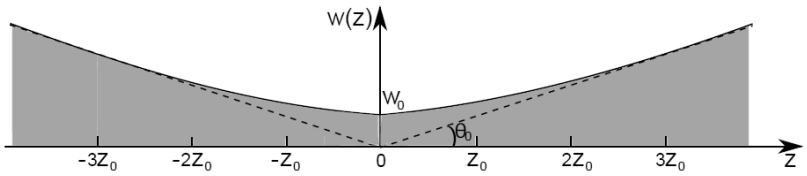

Figure 2.4: Performance of the radius of a Gaussian beam and its parameters. Image taken from [9].

2.4 Electromagnetic waves

Nowadays it is recognized that light is composed by photons and when dealing with a large number of photons, light can usually be treated like a classic wave. Let's start from a quote by Maxwell: *"[..] light and magnetism are affections of the same substance, and that light is an electromagnetic disturbance propagated through the field according to electromagnetic laws"*. It is important to underline how an electromagnetic wave is classified through its frequency (or through its wavelength from equation $c = \lambda f$). Light is defined as an electromagnetic wave with frequency in the visible region. Here this definition is extended to include the infrared spectrum, which is used in OCT imaging: typical wavelengths used to inspect non-transparent tissues are around 1300 nm (near infrared region).

2.4.1 Polarization

Polarization is an important property of an electromagnetic wave and OCT, in order to examine tissues and measure their interaction with light, uses polarization-sensitive detectors. Light can be represented with transversally oscillating electromagnetic fields; if we observe it propagating along the z-axis we can express the electric field as

$$\mathbf{E}_x(z,t) = \hat{\mathbf{x}} E_{0x} \cos(kz - \omega t + \epsilon_x), \tag{2.20}$$

or

$$\mathbf{E}_y(z,t) = \hat{\mathbf{y}} E_{0y} \cos(kz - \omega t + \epsilon_y), \tag{2.21}$$

where $\epsilon_{x,y}$ is the phase associated to each direction. If the difference $\epsilon = \epsilon_x - \epsilon_y$ is zero or a multiple of 2π the sum of the two fields is

$$\begin{aligned}\mathbf{E}(z,t) &= \mathbf{E}_x(z,t) + \mathbf{E}_y(z,t) \\ &= \hat{\mathbf{x}} E_{0x}\cos(kz - \omega t) + \hat{\mathbf{y}} E_{0y}\cos(kz - \omega t) \\ &= (\hat{\mathbf{x}} E_{0x} + \hat{\mathbf{y}} E_{0y})\cos(kz - \omega t).\end{aligned} \tag{2.22}$$

So the electric field forms a constant angle with the x-axis equal to

$$\phi = \tan^{-1}\left(\frac{E_{0y}}{E_{0x}}\right). \tag{2.23}$$

When $E_{0x} = E_{0y}$ the light is linearly polarized at an angle of 45 degrees with the x-axis. More generally, if $\epsilon = \pm k\pi$ the light is still linearly polarized but with a different inclination, which is determined by equation 2.23.
Now, if we consider the cases $\epsilon = \pm\frac{\pi}{2}$ equation 2.22 becomes

$$\mathbf{E}(z,t) = \hat{\mathbf{x}} E_{0x}\cos(kz - \omega t) \pm \hat{\mathbf{y}} E_{0y}\sin(kz - \omega t), \tag{2.24}$$

where the two waves are still not aligned and the electric field doesn't form a constant angle with the x-axis: its rotation along the x and y axes is a function of its position along the z-axis and time t. If $E_{0x} = E_{0y} = E$ the polarization is said to be circular because the amplitude of the light is the same at each point along z-axis. Two cases can be highlighted:

- if $\epsilon = +\frac{\pi}{2}$ we have clockwise polarization;
- if $\epsilon = -\frac{\pi}{2}$ we have left-hand polarization.

In all the other cases, where the two orthogonal waves are out of phase and $E_{0x} \neq E_{0y}$, the light has elliptic polarization and its intensity varies depending on the angle.

Tissues can interact with the state of polarization of light and all these changes can be described using either the Jones or Mueller approach.
The state of polarization of light can be defined with Jones vectors whereby the electric field is expressed in terms of amplitude and phase in the x and y components

$$\mathbf{E} = \begin{bmatrix} E_x \\ E_y \end{bmatrix} = \begin{bmatrix} E_{0x}\cos(kz - \omega t + \epsilon_x) \\ E_{0y}\cos(kz - \omega t + \epsilon_y) \end{bmatrix}. \tag{2.25}$$

This vector describes the state of polarization of light and each change can be expressed as the product of the Jones vector and the Jones matrix, a 2x2 matrix that contains all the information on the polarization changes induced by a material. The Mueller approach uses the Stokes vector instead of the Jones one. The components of the Stokes vector can be measured empirically and the vector itself can be written as

$$S = \begin{bmatrix} I \\ Q \\ U \\ V \end{bmatrix}, \tag{2.26}$$

where the quantities I, Q, U and V are respectively:

- I = total intensity;
- $Q = I_0 - I_{90}$, the difference between the intensity of the horizontal and vertical components of the polarized light;
- $U = I_{+45} - I_{-45}$, the difference between the intensity of the polarized components with orientation $+45°$ and $-45°$;
- $V = I_{rcp} - I_{lcp}$, the difference between the intensity of the right-hand and left-hand polarization components.

Any transformation of the states of polarization is now described by the Mueller matrix (4x4).
The Mueller approach has several advantages such as the use of easily measurable quantities, which can be used with non-polarized light, as in OCT systems where sources emit partially polarized light.

The Stokes vectors can be used to graphically represent a particular state of polarization on the Poincaré sphere (Figure 2.5).
This sphere can be divided into 3 parts:

- the upper hemisphere corresponds to light with elliptical left-hand polarization while the north pole represents the left-hand circular polarization;

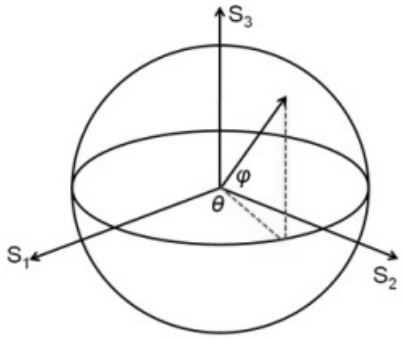

Figure 2.5: Poincaré sphere. Image taken from [13].

- the lower hemisphere corresponds to light with elliptical right-hand polarization while the north pole represents the right-hand circular polarization;

- the equator represents light with linear polarization.

Considering the average intensities of the states of polarization, the Stokes vector 2.26 can be written as

$$\mathbf{S} = \begin{bmatrix} S_0 \\ S_1 \\ S_2 \\ S_3 \end{bmatrix} = \begin{bmatrix} A_x^2 + A_y^2 \\ A_x^2 - A_y^2 \\ 2A_x A_y \cos\psi \\ 2A_x A_y \sin\psi \end{bmatrix}, \tag{2.27}$$

where A_x and A_y are the average amplitudes along the x and y directions at the detector and ψ is the phase difference between the two orthogonal fields. If we ignore the first Stokes parameter S_0, the other three can be plotted directly in three dimensional Cartesian coordinates. If we are not interested in the total beam power, as is usually the case, then we can use a normalized Stokes vector obtained by dividing the Stokes vector components by the total

intensity S_0:

$$\mathbf{S}' = \frac{1}{S_0} \begin{bmatrix} S_0 \\ S_1 \\ S_2 \\ S_3 \end{bmatrix}. \tag{2.28}$$

The normalized Stokes vector $\mathbf{S}'$ then has unitary power ($S'_0 = 1$) and the three significant Stokes parameters plotted in three dimensions will lie on the unity-radius Poincaré sphere for pure polarization states (where $P'_0 = 1$). Partially polarized states will lie inside the Poincaré sphere at a distance of $P' = \sqrt{S'^2_1 + S'^2_2 + S'^2_3}$ from the origin. When plotted, that point will lie on the surface of the unity-radius Poincaré sphere and indicate the state of polarization of the polarized component.

2.4.2 Fiber optics

An OCT system consists entirely of fiber optics components, such as patch cords, polarization beam splitters and optical couplers. Optical fiber technology is based on total internal reflection: the reflection index of the cladding is lower than the index of the core, in order to make internal reflection possible. Not all the waves propagate inside the fiber, because light has to hit the core-mantle interface below the critical angle to enter the core. Otherwise it enters the cladding where it can't propagate because of dispersion and losses through the walls of the fiber. This becomes clinically relevant, for example, when using catheters and endoscopes. Passing through the body changes the curvature of the fiber and can lead to leakage of light.

Fiber optics can be classified in single-mode fibers or multi-mode ones: a multi-mode fiber is characterized by a bigger core, it accepts waves with different input angles and the propagation is different for each mode. They follow different routes inside the core and it takes them different times to reach the end of the fiber, causing modal dispersion and increasing the noise at the detector. Using single-mode fibers it is possible to obtain a higher resolution: OCT uses this type of fiber where the light can follow only one route, without significant mode dispersion. Although single-mode fibers have

a higher resolution than multi-mode ones, the former are more difficult to couple and this typically results in a loss of power.

Optical fibers have a significant effect on the polarization of light. When we refer to single-mode, we actually consider the two modes defined by the two ortogonal states of polarization, which propagate indipendently along the fiber. The state of polarization is also influenced by the geometry of the fiber. Real fibers are not perfectly cylindrical and the two orthogonal states follow different paths with the consequent mode dispersion. Another factor that affects the state of polarization is the the curvature of the fiber, since the two modes travel different distances because they oscillate along different axes of the fiber. All these phenomena are known as polarization mode dispersion (PMD) and they reduce the OCT resolution.

Chapter 3

OCT: Theory

OCT requires a high acquisition rate to measure the retroreflected intensity, because of the high speed of light. For this reason it is not possible to use electrical devices and an interferometer has to be used instead. OCT systems can be implemented using several different technologies, which we can group in three broad categories:

- TD-OCT: Time Domain OCT. Historically the first technology to be developed, it uses a broad-spectrum light source to obtain a low coherence interference in order to measure the various distances between the internal structures of the tissue;
- FD-OCT: Fourier Domain OCT. Here the information is derived from the spectrum of the interference signal. We can further subdivide it into two categories:
  - SD-OCT: Spectral Domain OCT. Just like TD-OCT, it uses a broad spectrum light source;
  - SS-OCT: Swept Source OCT. The source is a laser, whose operating wavelength λ varies in the interval $\Delta\lambda$ and it is centred in λ_0.

For a detailed description of the first two technologies we refer to previous works [9, 10]. In the experimental part of this thesis we use an SS-OCT system, which differs from the other two setups for having a higher sensitivity and imaging depth [8], so we will focus on it in detail.

3.1 Swept Source OCT

SS-OCT [3, 6] uses interferometry in the frequency domain to retrieve information about the sample under investigation. Here intensities are measured sequentially, by lighting the interferometer with a tunable narrow-band laser and measuring the output intensity using either one or two photodiodes (as in the case of PS-OCT). As we can see in Figure 3.1 the two arms of the interferometer are connected to a reference mirror and to the sample under test respectively. The light reflected from both arms is combined at the detec-

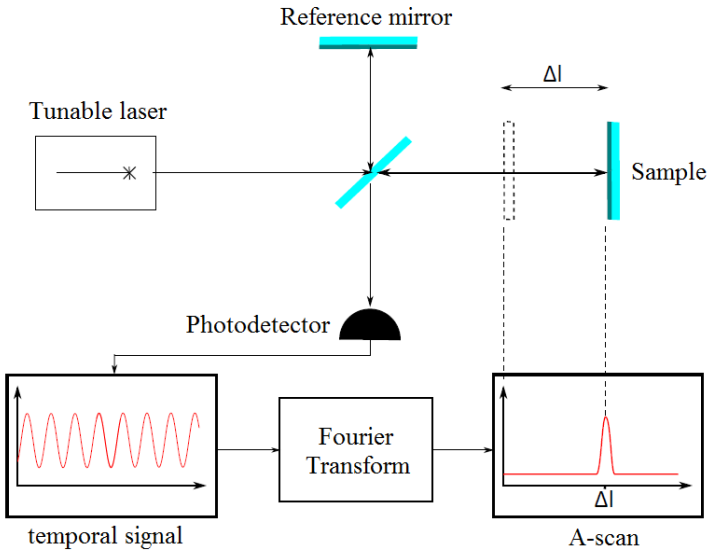

Figure 3.1: Image taken from [9]. SS-OCT system.

tor where we can observe the presense of beat, since the coherence length of the laser is much higher than the lengths of the system and the waves may interfere constructively. The light emitted by the source is linearly modulated, so that the waves that interact at the detector have different wavelengths, and their difference is proportional to the difference between the distances traveled by the two light beams. This difference produces a beat frequency, that is measured by the photodiode.

The tunable laser emits a signal with frequency $\nu(t)$ that varies over time. Such a signal is called a "chirp signal" and it is shown in Figure 3.2:

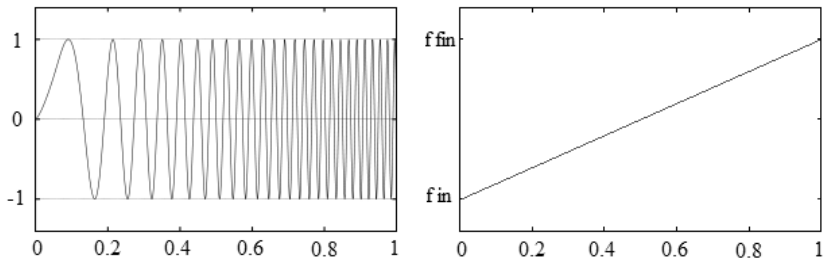

Figure 3.2: Chirp signal and its frequency time-course.

This particular signal is described by the equation

$$\begin{aligned} E_{so}(t) &= E_{so} \cdot e^{j2\pi\nu(t)t} \\ &= E_{so} \cdot e^{j\omega(t)t}, \end{aligned} \tag{3.1}$$

where $\omega(t)$ varies over time according to

$$\omega(t) = \omega_{in} + mt, \tag{3.2}$$

with $\omega = 2\pi f$ and therefore at the two ends of the interval we have

$$\omega_{in} = \omega(0) = 2\pi f_{in}, \qquad \omega_{fin} = \omega(T) = 2\pi f_{fin}. \tag{3.3}$$

We can also define the "chirp rate" as:

$$m = \frac{d\omega}{dt}. \tag{3.4}$$

From Figure 3.1 we can observe that the difference in length between the two arms of the interferometer is $\Delta l = |l_s - l_r|$ where l_s and l_r are the distances of the sample and the reference mirror from the interferometer, respectively. At time $t = t_i$ the laser emits light with instantaneous angular frequency $\omega(t_i)$ and the resulting wave is divided into two parts, which follow different paths in the system. Now we assume $l_s > l_r$ and we consider the interferometer at time $t = t_i + 2t_s$ where $2t_s$ is the time it takes the light to travel from the interferometer to the sample and back:

- the first interfering beam - which hit the sample - has covered the distance $2l_s$;

- the second light beam - which travelled the reference arm - has covered the distance $2l_r$ (accordingly to this it was emitted in a different instant $t_2 = t_i + \tau \neq t_i$).

Since the two distances are different, the waves that collide at the interferometer have different angular frequencies ω_s and ω_r

$$\omega_s = \omega(t_i), \tag{3.5}$$

$$\omega_r = \omega(t_i + 2t_s - 2t_r) = \omega(t_i + \tau), \tag{3.6}$$

where

$$\tau = 2t_s - 2t_r = \frac{2\Delta l}{c}. \tag{3.7}$$

These two waves, at time $t = t_i + 2t_s$, generate beat with frequency

$$\begin{aligned} \omega_b &= \omega_r - \omega_s \\ &= \omega(t_i + \tau) - \omega(t_i) \\ &= [\omega_{in} + m(t_i + \tau)] - (\omega_{in} + mt_i) \\ &= m\tau = m \cdot \frac{2\Delta l}{c}. \end{aligned} \tag{3.8}$$

The photodiode produces an electrical signal with angular frequency ω_b, proportional to the distance Δl: this distance can be calculated using the Fourier Transform. By applying it to the output of the photodiode, we obtain a peak (as we can see in Figure 3.1) that corresponds to ω_b on the frequency axis. Using equation 3.8 we can compute the value of Δl, which is proportional to the amount of power reflected back by the sample under investigation. We may observe more than one beat frequency, each of them corresponding to a different reflecting surface in the sample. Using the Fourier Transform we can identify their angular frequencies $\omega_{b,i}$, which are a function of the different distances travelled by light when going from the splitter to the i-th surface and back. The measurements we collect can be plotted against the depth in the z-axis to visualize all the different surfaces in the sample under examination. The graph we obtain is called A-Scan.
By repeating this procedure for different positions along a straight line and combining the results of each scan, we obtain a two-dimensional image called B-Scan. This can be done either by moving the sample, or through the use

of galvanometric mirrors which can change the direction of the light beam so as to make it hit different spots on the surface of the sample. By the same logic it is possible to create three-dimensional volumetric images combining different B-Scans, obtained by shifting the line traced by a B-scan in the orthogonal direction. The result of the operation is called C-Scan.

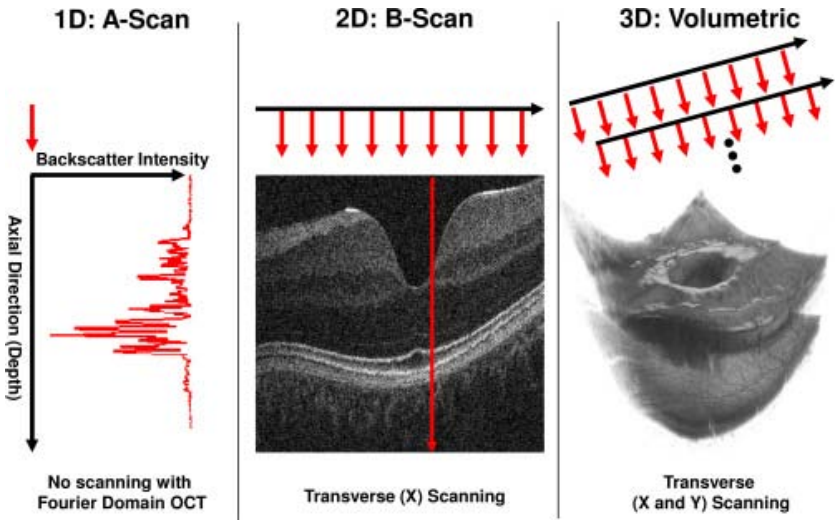

Figure 3.3: Examples of A-Scan, B-Scan and C-Scan. Image taken from [14].

3.1.1 Parameters

Wavelength range The iteration between light and the sample under analysis depends on the nature of the material. There are two main phenomena to consider:

- *scattering*: light is forced to deviate from a straight trajectory due to localized non-uniformities in the medium it travels through. This effect is more pronounced when wavelengths are smaller;

- *absorption*: as photons travel through non-empty space, they are absorbed by the matter they interact with, typically by electrons. Therefore, their electromagnetic energy is transformed into internal energy of the absorber, for example thermal energy. This reduction in the intensity of a light wave propagating through a medium is also called

attenuation, and it is usually independent of the intensity of the radiation.

Because of these two phenomena the power of the light beam decreases with depth, limiting the inspection to the maximum possible depth that can be reached with a specific type of light. In Figure 3.4 we can see that in ophthalmology wavelengths between 700 and 900 nm are the most effective, as they minimize the absorption caused by water. Wavelengths of about 1300 nm are used to obtain images of skin and arterial walls, as the amount of water in these tissues is limited, so absorption and scattering are reduced. Other wavelengths, from 1500 nm to 1700 nm, can be used to achieve greater depth where the attenuation caused by the presence of water is not a limiting factor.

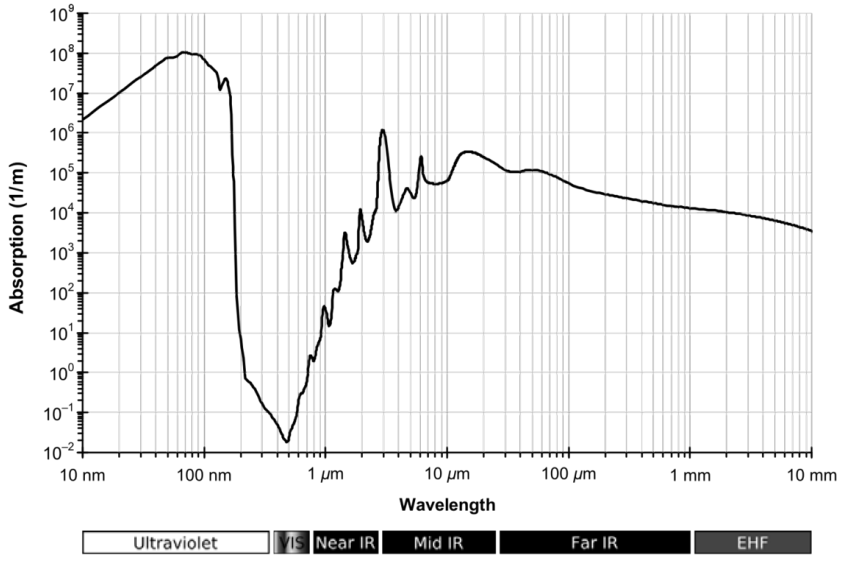

Figure 3.4: Absorption spectrum of water. Image taken from [15].

Axial resolution This is one of the most important parameters and it represents the ability to distinguish two different points along the longitudinal z-direction. It depends on the source of light that is used and in particular on the Fourier Transform of its power spectrum. For a broad-spectrum source axial resolution depends on its coherence length; if its power spectrum follows

a Gaussian distribution it can be demonstrated [8] that its axial resolution is

$$\Delta z = \frac{2\ln(2)}{\pi}\frac{\lambda_0^2}{n\Delta\lambda}, \tag{3.9}$$

where n is the refraction index of the medium. In our setup the source has a rectangular spectrum, and its axial resolution is

$$\Delta z = \frac{\lambda_{min}\lambda_{max}}{n\Delta\lambda}. \tag{3.10}$$

We can observe that as we increase the bandwidth $\Delta\lambda$, the resolution greatly improves and with specific sources it is possible to achieve a resolution of up to 1 μm. In Figure 3.5 we compare the results obtained with three different resolutions.

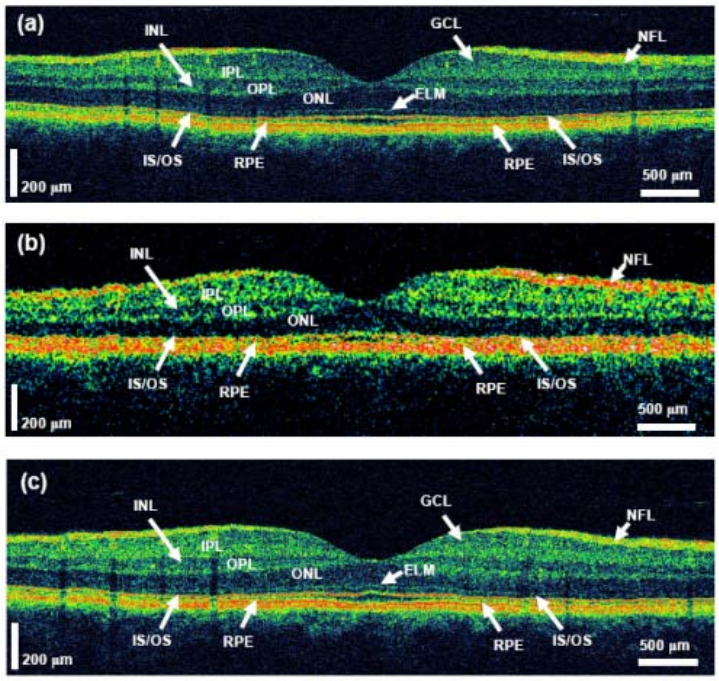

Figure 3.5: OCT images of normal retina taken from the same location, using different axial resolutions: a) ~ 3.4 μm b) ~ 10 μm c) ~ 3 μm. Image taken from [16].

Transversal resolution While axial resolution is determined by the optic source, transversal resolution depends on the light beam and its focusing on

the sample. This quantity is equal to the radius of the beam where the focus is maximum and it is the same as the "waist beam" in the case of a Gaussian beam. From [17] we can compute the transversal resolution as

$$\begin{aligned} \Delta x &= \frac{\lambda}{\pi W_{nf}} f \\ &\simeq \frac{\lambda}{\pi NA}, \end{aligned} \tag{3.11}$$

where W_{nf} is the radius of the unfocused beam before the lens and NA is the numerical aperture of the lens used to focus the beam. So, equation 2.18 can be rewritten as

$$\begin{aligned} 2z_0 &= \frac{2n\pi\Delta x^2}{\lambda} \\ &= \frac{2\lambda}{\pi NA^2} = \frac{2\lambda}{\pi W_{nf}^2} f^2, \end{aligned} \tag{3.12}$$

where n is the refraction index of the material. It is easy to see the correlation between transversal resolution and depth of focus: a higher numerical aperture improves transversal resolution but it also decreases the depth of focus which leads to a lower quality image in the z-axis. It is common to use a fixed transversal resolution of about 10-15 μm in order to have a higher depth of focus (about 2-3 mm).
It is also possible to increase the total resolution of the image using adaptive-optic systems [18, 19]: here the depth of focus is sacrificed in order to obtain the highest possible transversal resolution. Then the sample is moved along the z-axis and the measure repeated. Finally, with the use of appropriate algorithms, the acquired images are merged together to obtain an image with both high transversal and axial resolutions.

Sensitivity and speed of acquisition With OCT technologies the quality of images is strictly dependent on the sensitivity of the system and its detectors. Sensitivity is defined as the ratio between the emitted signal and the minimum measurable reflectivity of the sample. This last quantity is also equal to the noise power, which in turns depends on the sources of noise in the system.

If we consider the different power reflected by the two arms (reference mirror and sample) it is clear that the reference arm has a higher power than the sample one. One of the peculiarities of OCT is the use of an interferometer: the power measured by the detector is the sum of the power received from the two arms. So, the signal received from the sample, usually very small, is multiplied by the reference one and then the total interference signal measured by the detector is enhanced. Standard OCT systems have sensitivities of about $90 \div 100$ dB.

One possible way to improve the sensitivity of the system is to use a higher incident power to increase the reflected one. But when doing that care must be taken to conform to the standards on safe exposure limits defined by the American National Standards Institute (ANSI). These standards determine the maximum power that can be used as a function of wavelength and exposure time. The incident power per square millimeter must be kept below the ANSI limits in order not to damage the sample under test.
Another possibility is to reduce the scanning time per A-Scan. The combination of reduced total scanning time and higher scanning speed enables the use of higher optical power without changing the total amount of energy that hits the sample. This results in both higher sensitivity and greater depth.

3.2 PS-OCT

Standard OCT is not polarization-sensitive, because it only makes use of the intensity of the reflected light, without taking into account the changes to its state of polarization. But some types of tissue, in particular those within highly organized structures, are very sensitive to polarization and they are able to change the polarization of the light they reflect. Taking advantage of these properties is the basis of PS-OCT technologies.

PS-OCT is complementary to standard OCT technologies: while OCT is used to determine the internal structure of a biological sample, PS-OCT helps us identify its detailed biochemical composition. It allows us, for example, to find highly organized molecules in actin-myosin structures, cholesterol crystals, collagen (found in cartilage), tendon, bone, corneas, and several other parts of the body. Biological substances change the polarization of

incident light through birefringence, dichroism and optical rotations.
Birefringence is the optical property of a material whose refractive index depends on the state of polarization and the direction of propagation of light. It is responsible for the phenomenon of double refraction whereby the polarization components of a ray of light, when incident upon a birefringent material, are split and made to follow slightly different paths. Dichroism is characterized by the different levels of attenuation that affect light in different states of polarization: for example, light linearly polarized along a particular axis may be attenuated while light polarized along the ortogonal direction may not be affected. And finally, there are other molecules that can actually rotate the state of polarization of light.
PS-OCT exploits birefringence to obtain additional information about a sample: in particular birefringence is usually observed in anisotropic crystals but it can also occur in optically isotropic materials under certain specific conditions:

- *stress birefringence*: it arises when external forces are applied to isotropic materials so that the isotropy is lost in one direction;
- *intrinsic birefringence*: whereby the material has more than one chemical group with differing refractive indices that have a preferential order that results in optical rotation;
- *form birefringence*: whereby structure elements, such as rods or spheres having one refractive index, are suspended in a media with a second refractive index;
- by the self or forced alignment into thin films of amphiphilic molecules such as lipids, some surfactants or liquid crystals.

Birefringence is also used in medical diagnostics: in ophthalmology, binocular retinal birefringence screening of the Henle fibers provides a reliable detection of strabismus, while birefringence of the optic nerve fibre layer can be used to indirectly quantify its thickness, which is of use in the assessment and monitoring of glaucoma. Also birefringence of particles biopsied from pulmonary nodules indicates silicosis. Therefore, PS-OCT could potentially be a powerful clinical technology.

3.2.1 Birefringence theory

The state of polarization of light can be represented in a three dimensional space (section 2.4.1) through the unitary Stokes vectors [20]. The SOP of light at an arbitrary position inside the fiber can be written as

$$\hat{s}(z) = \mathbf{F}(z)\hat{s}_0, \tag{3.13}$$

where z is the position along the axis of the fiber and $\hat{s}_0$ is the unitary Stokes vector that represents the state of polarization of light at the input end of the fiber. $\mathbf{F}(z)$ is the 3x3 real Mueller matrix that describes the polarization changes during the propagation of light: it represents the rotations in the three-dimensional Stokes space. In particular, any change of $\mathbf{F}$ with respect to z can be written as

$$\frac{d\mathbf{F}}{dz} = \bar{\beta}(z) \times \mathbf{F}(z), \qquad \mathbf{F}(0) = \mathbf{I}, \tag{3.14}$$

where $\mathbf{I}$ is the identity matrix, and $\bar{\beta}(z) = (\beta_1, \beta_2, \beta_3)^T$ is the birefringence vector, a mathematical quantity that describes the local effects of all the perturbations that act on the fiber at z. It consists of two different components, a linear one and a circular one. Using equation 3.13 we obtain

$$\frac{d\hat{s}}{dz} = \bar{\beta}(z) \times \hat{s}(z), \qquad \hat{s}(0) = \hat{s}_0. \tag{3.15}$$

Similarly, we can define another Mueller matrix $\mathbf{R}(z)$ to represent the round-trip propagation of light from the input end of the fiber to the sample ($\mathbf{F}$) and back ($\mathbf{B}$) as

$$\mathbf{R}(z) = \mathbf{B}(z)\mathbf{S}\mathbf{F}(z), \tag{3.16}$$

where $\mathbf{S}$ represents the retroreflection of the sample. If the fiber is mutual we can write:

$$\mathbf{B} = \mathbf{M}\mathbf{F}^{\mathbf{T}}\mathbf{M}, \qquad \mathbf{M} = \begin{bmatrix} 1 & 0 & 0 \\ 0 & 1 & 0 \\ 0 & 0 & -1 \end{bmatrix}. \tag{3.17}$$

The round-trip birefringence vector $\beta_R(z)$ can be written as

$$\frac{d\mathbf{R}}{dz} = \bar{\beta}_R(z) \times \mathbf{R}(z), \qquad \mathbf{R}(0) = \mathbf{I}, \tag{3.18}$$

$$\frac{d\hat{s}_R}{dz} = \bar{\beta}_R(z) \times \hat{s}_R(z), \qquad \hat{s}_R(0) = \hat{s}_0, \tag{3.19}$$

where $\hat{s}_R(z)$ can be measured with a polarization sensitive reflectometer. Both $\bar{\beta}(z)$ and $\bar{\beta}_R(z)$ are affected by the perturbations light encounters along the fiber. As explained in [20], we can use well-known algorithms [21, 22] to calculate the roundtrip birefringence vector $\bar{\beta}_R(z)$. The precise relationship between $\bar{\beta}_R(z)$ and $\bar{\beta}(z)$ is not obvious, and it takes a few calculations to prove that

$$\bar{\beta}_R(z) = 2\mathbf{B}(z)[\bar{\beta}_L(z) + \eta(z)\hat{u}_3], \tag{3.20}$$

where $\eta(z) = 2\mathbf{VB}(z)\cos\psi(z)$ is the Faraday rotation and $\bar{\beta}_L(z)$ is the linear component of the birefringence vector $\bar{\beta}(z)$. The roundtrip birefringence vector $\bar{\beta}_R(z)$ is not a local quantity; on the contrary, it depends (via the term $\mathbf{B}$(z)) on the physical properties of the whole section of fiber that goes from the input end of the cable to the scattering point. Despite the presence of $\mathbf{B}$(z) in 3.20, it is still possible to obtain partial information on local birefringence by noting that $\mathbf{B}$(z) is an orthogonal matrix, and hence

$$|\bar{\beta}_R(z)| = 2\sqrt{|\bar{\beta}_L(z)|^2 + |\eta(z)|^2}. \tag{3.21}$$

This relationship is particularly useful when the Faraday rotation is negligible ($\eta \simeq 0$), which is quite common. Equations 3.19 and 3.21 state that the speed at which the backscattered SOP varies at an arbitrary position z, is proportional to twice the modulus of linear birefringence at that same position. Since the unit vector $\hat{s}_R(z)$ is constrained to a spherical surface (the Poincaré sphere), its variations are generally limited to oscillations; therefore, the speed of variation, and hence the absolute value of the local linear birefringence, can be computed with a simple spectral analysis. This simple analysis, however, cannot give us complete information on birefringence. In particular, at this stage we have no knowledge about the orientation of $\bar{\beta}_L(z)$. To this aim, a more detailed analysis is required, but this goes beyond the purpose of this thesis.

Chapter 4

Experimental setup

We are now going to describe the components of the two setups we tested. We will start from the components and settings of a standard SS-OCT system, and then we will explain how we implemented our polarization-sensitive OCT.

4.1 SS-OCT

4.1.1 Components

OBR

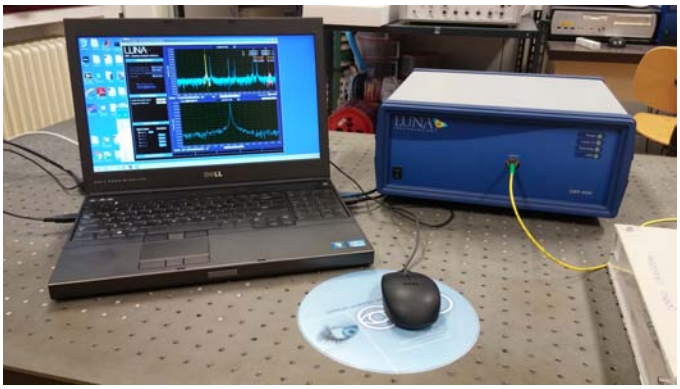

Figure 4.1: OBR device.

This device (Figure 4.1) was built by Luna Technologies Inc. and uses

swept-wavelength coherent interferometry to measure minute reflections in an optical system as a function of length, including both phase and amplitude information: the amplitude of the time domain data is equivalent to a traditional optical time domain reflectometry (OTDR) measurement. Specifically, it compares the signals reflected by the device under test (DUT) and the reference arm (Figure 4.2).

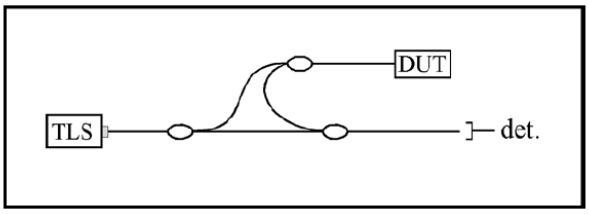

Figure 4.2: OBR device scheme. Image taken from [23].

Their overlap may produce interference and beat; the OBR measures the frequency of the signal with a Fourier Transform and uses it to obtain the delay τ between the signals. This delay is the difference between the times it takes the two beams of light to travel their respective paths. Then it computes the corresponding distance using

$$z = \frac{c}{2n}\tau, \tag{4.1}$$

where c is the speed of light in vacuum, n is the refraction index of the system and z is the extra (compared to the reference arm) one-way distance travelled by the light that hits the DUT. The choice of n is very important, as the distances shown by the device (using a dedicated proprietary software) depend on the speed of the light in the DUT. The axial resolution of the device is also related to the refraction index as seen in equation 3.10:

$$\Delta z = \frac{\lambda_{min}\lambda_{max}}{n\Delta\lambda}.$$

In our tests we chose to set the refraction index to $n_{ref} = 1$, because in our case light interacts with air and samples composed by different layers with different refraction indexes. So we had to choose a single value that defines the worst-case resolution: in practice, samples will certainly have higher refraction indexes and consequently higher resolution too.

The OBR can be controlled remotely, using either GPIB or TCP/IP commands via an IEEE 802 interface. We chose to use TCP/IP commands that are sent to the device using Matlab native functions. Its specifications are listed in Table 4.1.

Table 4.1: OBR details.

Parameters	**Value**
Sensitivity	-130 dB
Dynamic range	70 dB
Wavelength range	1500-1650 nm
Maximum Device Length	30 or 70 meters
Spatial Resolution	10 μm over 30 meters

Optical unit

Figure 4.3: AC254-060-C-ML lens. Image taken from [24].

The lenses (Figure 4.3) we used are two identical AC254-060-C-ML (Thorlabs Inc.), with the following specifications:

- material N-LAK22/N-SF6HT;
- Positive IR Achromatic Doublets;
- AR Coated for the 1050 - 1620 nm Range;

- diameter $d = 25.4$ mm;
- numerical aperture $NA = 0.22$;
- focal lenght = 60.0 mm $\pm 1\%$.

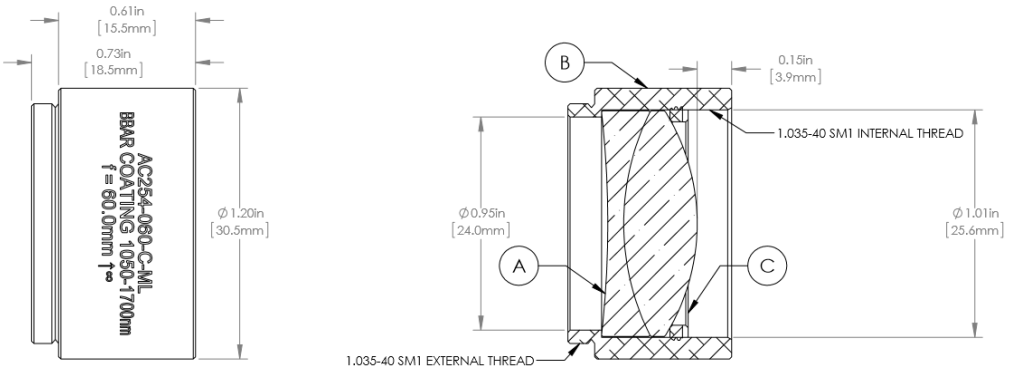

Figure 4.4: Physical dimensions of the lens. Image taken from [24].

AR coating reduces the power reflected by the surface of the lens. That is helpful when dealing with low-power signals such the intensity of the light reflected back by the sample. These lenses are achromatic doublets: they can effectively limit chromatic aberration and are frequently used to achieve a diffraction-limited spot when using a monochromatic source like a laser. They are composed of two layers made by different types of glass (N-LAK22 and N-SF6HT) in order to reduce the "focal shift", the drift of the point of focus that occurs as the wavelength varies. This is a very important property for us because we will be working with a broad range of wavelengths and we want the position of the "waist beam" to be as stable as possible. In Figure 4.5 we can find the building specification for each lens.

Translator and Control Module

In order to generate a B-Scan of a sample we must combine multiple A-Scans taken in different positions. The two main methods that are commonly used are:

- the beam is deflected with the use of a galvanometer mirror;

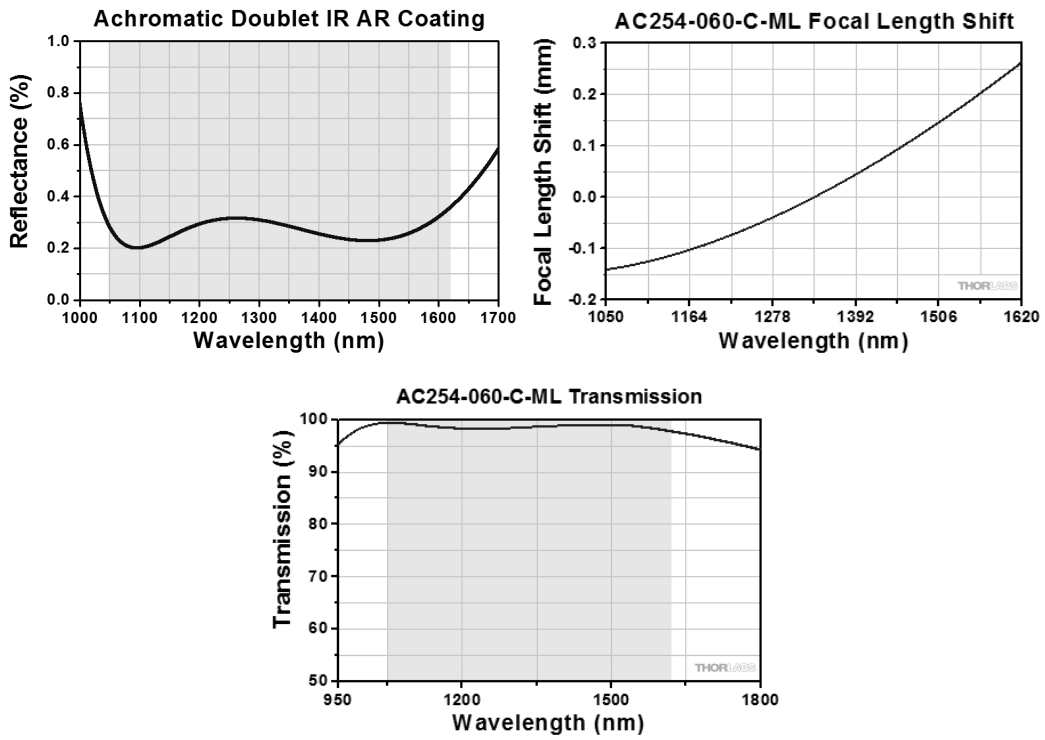

Figure 4.5: Specification on the reflectivity (a), focal shift (b) and theoretical transmission (c). Image taken from [24].

- the beam is fixed while the sample is moved by an amount equal to the transversal resolution.

In our two setups we used piezoelectric shifters to move the sample. The specific device we used is a Burleigh CE-2000 3-AXIS 2mm/sec 10nm Command Module (Figure 4.6), that consists of the following components:

- Command Module CE-2000, which handles the user controls and sends them to the Translators;
- Inchworm Translators, which physically execute the Command Module commands and move the sample;
- Heidenhain Encoders, which reads the actual position of the sample relative to a fixed reference;
- Translation stage TS-100, the structure that contains the sample.

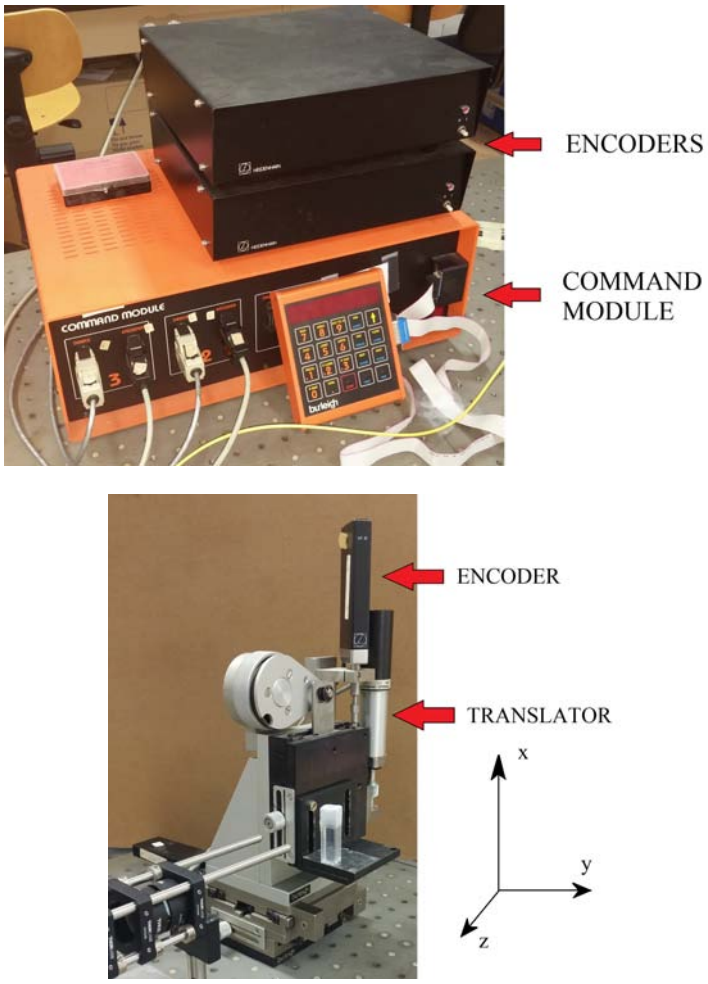

Figure 4.6: Translator device.

This system allows to precisely control the position of the sample, with a maximum shift of about 25 mm. It is possible to choose between a fixed-step shift mode (minimum value 0.1 μm) or a continuous one.

As with the OBR, the entire translator module is remotely controlled via a GPIB interface. With Matlab we were able to coordinate and synchronize the shifting of the sample, the OBR acquisitions and the data processing.

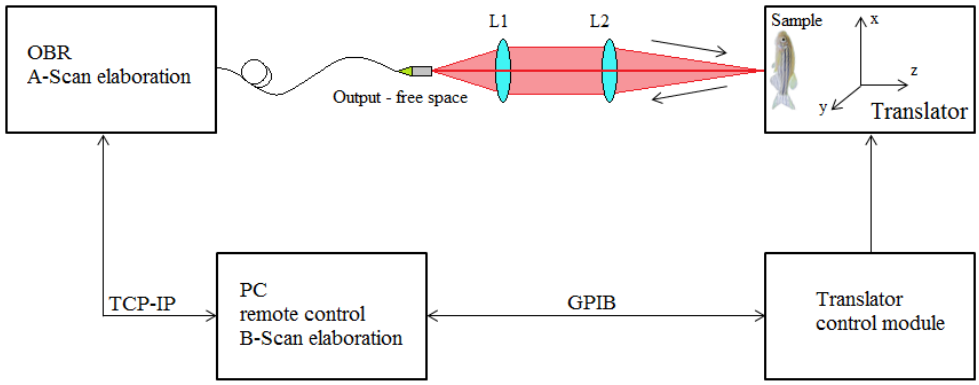

Figure 4.7: SS-OCT setup.

4.1.2 Experimental setup

In this OCT configuration, the OBR acts as swept-source and generates the laser radiation whose wavelength varies over an interval $\Delta\lambda$. The emitted light travels through the optical fiber and reaches the sample after a free space propagation during which the lenses are used to modify the geometry of the outgoing radiation. As we can see in Figure 4.7, the light emitted by the laser has to reach the sample and this is possible only if the last part of the propagation takes place in free space. To obtain the coupling between fiber and air and vice versa we used the lenses described in section 4.1.1: their purpose is to get the reflected light back into the fiber, in order to bring the information it carries to the OBR. The position of the lenses determines the width of the waist, the distance of the waist from the second lens and the focus depth: the sample is placed in the position that according to the theory leads too the highest resolution and the best inverse coupling between air and fiber.

The OBR is connected to the optical group with a 2-meter patch-cord whose free end is treated with an anti-reflection coating in order to minimize the reflection of the backscattered light at the air/fiber interface. The radiation leaving the fiber has an initial diameter equal to the core diameter (8.2 μm) and diverges with a semi-angle of 8.05°. This beam is collimated by the first lens and then focused on the sample by the second one: the same thing

happens to the beam reflected back from the sample.
The precise alignment of the lenses with the radiation coming from the fiber is necessary to hit the correct spot on the sample under test and to determine the exact position of the transversal plane of the waist. This requirement was satisfied using special cage plates, joined together with four bars and fixed on a workbench with anti-vibration supports. With this arrangement the lenses and the fiber are positioned on the same longitudinal axis along which we expect the light to propagate. The whole system is show in Figure 4.8.

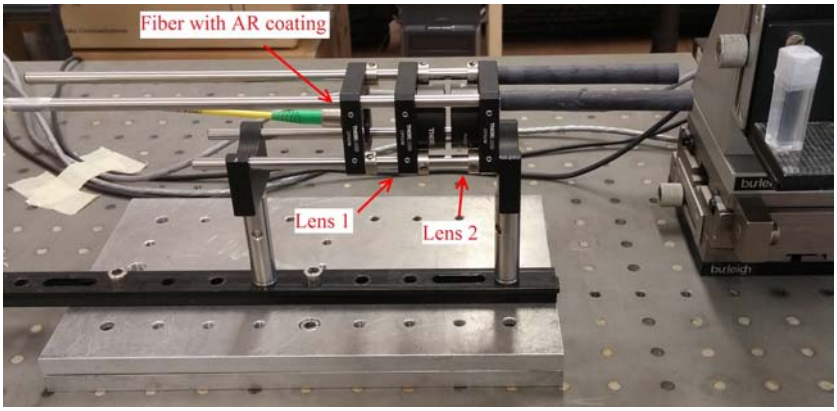

Figure 4.8: Optical group.

The information carried by the light reflected by the sample is analysed and post-processed by the OBR in order to obtain the reflectivity of the sample as a function of depth z, an artefact known in the technical literature as A-Scan. In order to obtain a two-dimensional image of the sample, several A-Scans have to be acquired and merged together in a single B-Scan (which is a bi-dimensional image). This is achieved by moving the sample with the Burleigh translator shown before. Acquisition times depend on the operating wavelengths (the bigger $\Delta\lambda$ is, the longer the time) and the number of A-Scans that are taken.

The entire system is controlled remotely via GPIB and TCP/IP commands. Matlab code is used to synchronize the various operations and to automate the movement of the sample between two successive A-Scans. Then the data have to be processed and merged to obtain the desired intensity images. The choice of operating wavelengths is limited by the operating

range of the source: $\Delta\lambda = [1525 \div 1610.85]$ nm $= 85.85$ nm with central wavelength $\lambda_0 = 1566.75$ nm. However, as seen in section 3.1.1, wavelengths from 1500 nm to 1700 nm are not very appropriate for samples that have a high water content because of water's high absorption and scattering in this particular range of wavelengths: this results in lower-quality images. The axial resolution, as calculated from equation 3.10, is

$$\Delta z = \frac{\lambda_{min}\lambda_{max}}{n_{air}\Delta\lambda} \simeq 28.61\ \mu m, \tag{4.2}$$

where we chose n_{air} as common reference. The axial resolution so calculated is referred to air. We can write the actual resolution inside the sample as $\Delta z_{sample} = \Delta z / n_{sample}$; considering that biological samples usually have refraction indexes between 1.3 and 1.5 we obtain an axial resolution of about 19-22 μm. Another important parameter is the transversal resolution, which is independent from the axial resolution and represents the transversal shift of the sample that we need to obtain a correct image of it. We know that this resolution corresponds to the minimum radius of the beam, also known as beam waist. In particular, reusing the setup built in previous work [9], the waist radius is equal to 15.82 μm at a distance of 134.63 mm from the second lens. This is obtained positioning the output end of the optical fiber at a distance of 29 mm from the first lens and choosing a distance between the two lenses of 4.78 mm. This configuration yields a focus depth of about 1 mm.

The following is the algorithm used to acquire and build the B-Scan image with this OCT configuration:

```
Data: transversal resolution and number of measures
Result: B-Scan image
initialize the OBR and the translator;
take first A-Scan and save its raw data;
for as many times as the number of required measures do
    take A-Scan at the current position;
    process previous data and save the result;
    while A-Scan is not completed do
        wait;
    end
    save current raw data;
    move the sample to the next position;
    if last measure then
        process data and save the result;
    end
end
move the sample to the initial position;
display the image obtained from processed data;
```

Algorithm 1: B-Scan acquisition.

4.2 Polarization Sensitive SS-OCT

4.2.1 Components

This system configuration (Figure 4.9) reuses the source (OBR), Burleigh Command Module and translator of the previous one. Several other passive devices are added to the system to build a PS-SS-OCT and in the following paragraphs we will describe their most important specifications.

Polarization Beam Splitters

To assemble our PS-OCT system we used two POBS-15-L-3-7-2 polarization beam splitters by AFW Technologies. They can divide the input signal into two orthogonal polarization components that are channelled into different output fibers (PBS 1) or combine the same two components into one output fiber (PBS 2). The splitters use PM panda fibers for the input and the output and provide a high extinction ratio with low loss. Their main

specifications are shown in Table 4.2.

Table 4.2: PBS specifications.

Parameters	**Value**
Connectors	FC/APC
Operating wavelength	1550 nm
Insertion loss	<0.6 dB
Pigtail type	900 μm
Pigtail Length	0.75 m
Return loss	>50 dB
Light path for combiner	port1 slow axis -> port3 slow axis
	port2 slow axis -> port3 fast axis
Light path for splitter	port3 slow axis -> port1 slow axis
	port3 fast axis -> port2 slow axis

Circulators

In the implementation of PS-OCT, two circulators are used to separate the forward and return path of the light. This is because the two orthogonal polarization states in which the input light is divided must reach the OBR at two different times. So, the OBR measures two different overlapping signals, each of them representing the response of the sample when illuminated with different states of polarization. In Table 4.3 we show their specifications.

Polarization Controller

In our setup we used a ProtoDel mechanical polarization controller which provides complete Poincaré sphere coverage by adjusting the angles of the

Table 4.3: Circulator specifications.

Parameters	**Value**
Connectors	FC/APC
Operating wavelength	1525 - 1610 nm
Max output power	500 mW
Note	low PDL and PMD

paddles. The design uses three wave plates with fixed retardation and variable orientation angles to control the state of polarization of the input light at the first polarization beam splitter in order to equally divide the power between the two paths (and then between the two states of polarization).

Polarization-maintaining optical fiber (PMF)

Between the two polarization beam splitters we used a polarization maintaining optical fiber (SM15-PS-U25A) in order to separately analyse the two orthogonal polarization components and their interaction with the sample. In this way the two components are forced to travel paths of different lengths, and their light, after being reflected by the sample, reaches the OBR at different times. Its specifications are listed in Table 4.4.

4.2.2 Experimental setup

In designing our PS-OCT system, we took advantage of the fact that polarization is easily influenced by the external environment [20]. In single mode fibers, every small perturbation that modifies the symmetry of the fiber can mix the two fundamental modes and change the polarization of the light. Our aim is to measure the state of polarization of the reflected light. This can be done by separating the forward and backward path of the light. The OBR then extracts the information about phase and amplitude of the two components that we need to calculate the state of polarization

Table 4.4: Polarization-maintaining optical fiber data sheet.

Parameters	**Value**
Connectors	FC/APC
Operating wavelength	1550 nm
Pigtail type	900 μm
Length	5 m
Chromatic dispersion	<3 ps/nm/Km

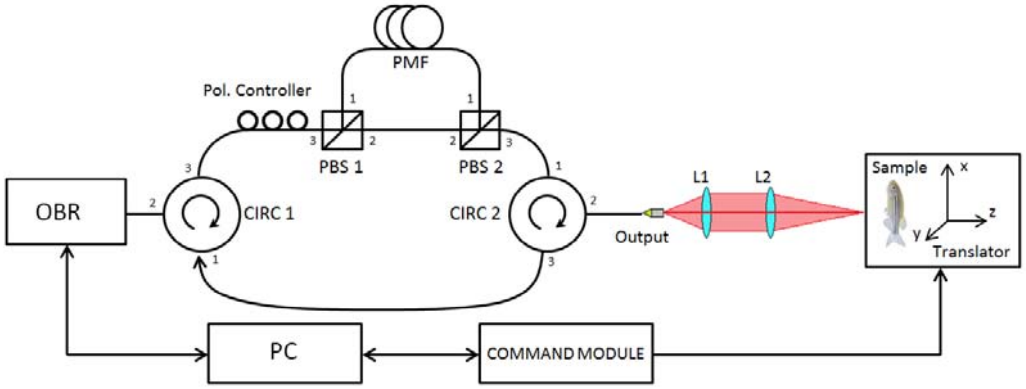

Figure 4.9: Polarization sensitive SS-OCT setup.

(SOP). In order to have complete information on the response of the sample to polarized light, we need to hit the sample with at least two different SOPs.

The system has two different light paths, one for each of the two random SOPs: these states of polarization depend respectively on the inputs of the fast and slow axes of port 3 of the first beam spitter. In order to fully study the birefringence of the sample we only have to analyse the retroreflected light, and we don't need any information about the incident one. But we need to measure the response of the sample to at least two different and non-orthogonal SOPs. That's because a necessary condition to obtain reliable information on birefringence is that the Stokes vectors of the two SOPs are not parallel or antiparallel in their representation on the Poincaré sphere.

In our setup we have two orthogonal polarizations - which correspond to antiparallel vectors on the Poincaré sphere - because of the presence of the two beam splitters and so we need to modify one of these SOPs in order to satisfy that requirement. To that end, we designed the system so that it would be able to automatically detect the two incoming signals and to modify one of the two states so as to obtain non-orthogonal polarizations. Specifically, we simulated the passage of the second beam of light through a quarter-wave plate that turns linear polarization into a circular one. This modification is obtained by multiplying its measured Jones vector by the matrix

$$\mathbf{T} = \begin{bmatrix} 1 & 0 \\ 0 & j \end{bmatrix}. \tag{4.3}$$

The algorithm used to acquire and build the B-Scan image with this OCT configuration is reported below.

We also measured the frequency response of the setup by adding a patchcord with FC/APC connectors at the end of the sample arm, where the sample itself should normally be. This causes a reflection of the signal that hits the connector, which it is then detected by the OBR. This is an unusual choice, but using a hybrid patchcord with FC/PC end connectors resulted in a reflected signal whose intensity was enough to saturate the receiver. The Fourier transform of the two signals that we measured are impulses whose positions depend on the different distances travelled by the corresponding SOPs. Figure 4.10 shows the return losses for the two states of polarizations, for both the total intensity and the two orthogonal polarizations x and y.

With the use of the software that comes with the OBR we can analyse the reflection caused by the FC/APC connector, and measure its return loss. The figure shows the (small) attenuation of the total intensity as a function of the wavelength, and the different magnitude of the attenuation for the two orthogonal components that causes a distortion of the state of polarization.

Data: transversal resolution, number of measures and positions of the two signals corresponding to the two SOPs
Result: B-Scan images for both the SOPs
initialize OBR and translator;
take first A-Scan;
save raw data for first SOP;
save raw data for second SOP;
for *as many times as the number of measures* **do**
  take A-Scan of the current position;
  process previous data and save the result;
  while *A-Scan is not completed* **do**
    wait;
  end
  save raw data for first SOP;
  save raw data for second SOP;
  move the sample to the next position;
  if *last measure* **then**
    process data and save the result;
  end
end
move the sample to the initial position;
display the images obtained from data processed;

Algorithm 2: B-Scan acquisition for PS-OCT.

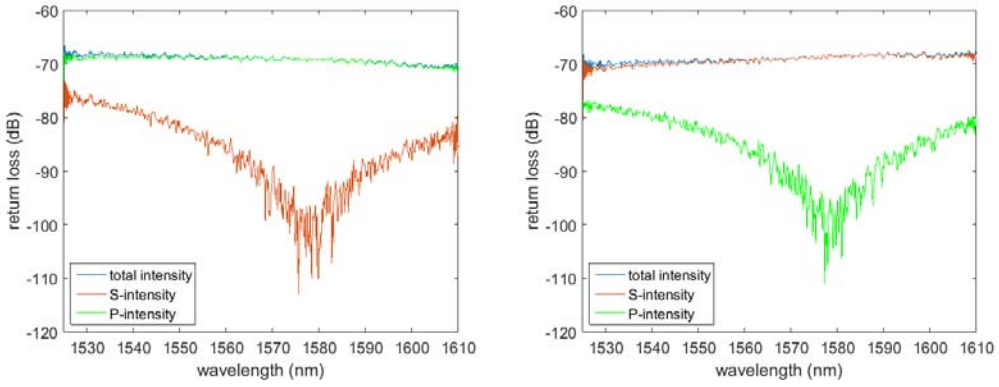

(a) SOP 1 (b) SOP 2

Figure 4.10: Return loss for each reflection peak.

Chapter 5

Results

5.1 Preliminaries analyses: SS-OCT

We used the system we built to analyse different samples. The purpose of these analyses was to get two-dimensional images (B-scan) of a given sample and to optimize the system for the study of samples of zebrafish. We first determined the relevant parameters of the setup by analysing the reflections produced by the lenses and the optical fiber links. Then we tested it on a couple of samples with a simple internal structure, a cuvette and a roll of adhesive tape. Finally we studied several suspensions in order to identify the substance best suited to our later analyses. The biological samples were prepared by Prof. Natascia Tiso of the Developmental Biology Lab (Department of Biology - University of Padova), in agreement with the authorization CEASA - project 407/2015-PR - of the University of Padova.

5.1.1 Characterization of the optical system

In order to determine the parameters of the system the first thing to do is to acquire an A-Scan in carefully controlled conditions. The signal that we measure shows a number of peaks, each of them representing a different device or element of the setup. There we can accurately measure the distances between the peaks and then determine the distances between the corresponding elements.

Optical group

Here we present the analysis of the optical group shown in section 4.1.2. In Figure 5.1 we can see all the reflections due to the lenses and the multiple air/fiber and air/glass couplings.

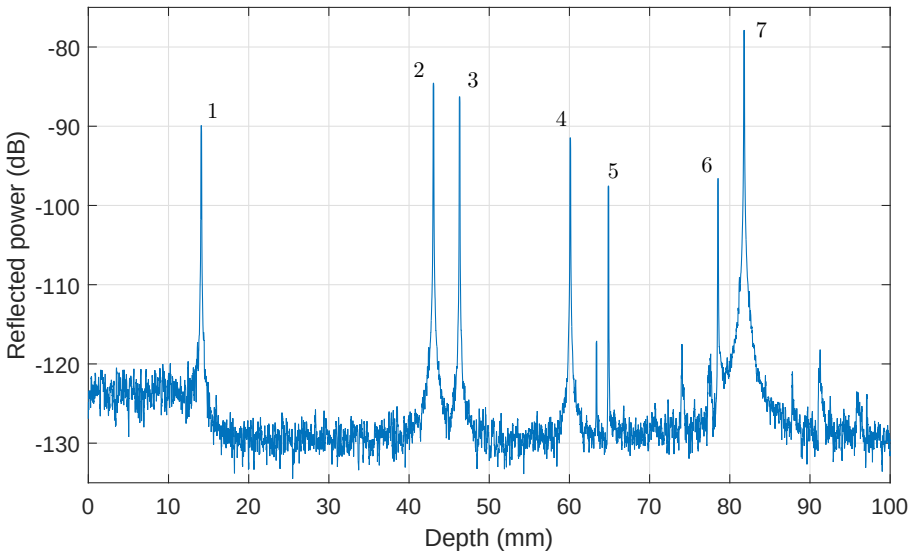

Figure 5.1: A-Scan of the optical group. The x-axis is normalized and it doesn't represent the real relative position of the elements identified by the OBR.

From the trace we can identify 7 different peaks, each of them representing a step-index between two different materials. The first peak corresponds to the exit of the beam from the fiber: we can identify it through its position (before the normalization) relative to the OBR and from the change in the attenuation factor. After this peak the background noise is lower than it was before and this represents a change of propagation medium. Peaks 3, 4 and 5 represent the first lens of the optical unit:

- peak 3: reflection due to the air/glass interface (N-SF6HT) of the lens;
- peak 4: the lens is an achromatic doublet and this is its internal reflection caused by the interface between the two types of glass N-SF6HT/N-LAK22;

- peak 5: reflection at the glass(N-LAK22)/air interface.

The last three peaks correspond to the second lens which is, in this case, inverted with respect to the first one.

The distances measured from the trace and the OBR are not the real ones. As we said before (section 4.1.1), the measurements are done using the common reference $n_{ref} = n_{air} = 1$: this implies that the distances read are referred to a homogeneous medium with refraction index equal to 1. To obtain the actual distances inside the lenses we have to denormalize them according to the relationship

$$d_{real} = d_{measured} \cdot \frac{n_{ref}}{n_{medium}} = \frac{d_{measured}}{n_{medium}} \tag{5.1}$$

that is easily obtained from equation 4.1.

5.1.2 First sample: cuvette

The first item we are going to characterize is a cuvette, a plastic container with a square base that is suitable for the analysis of samples in spectrophotometry. Samples can be positioned in the empty space between its plastic walls. This container, as we can see in Figure 5.2, has a simple structure whose elements are easy to identify.

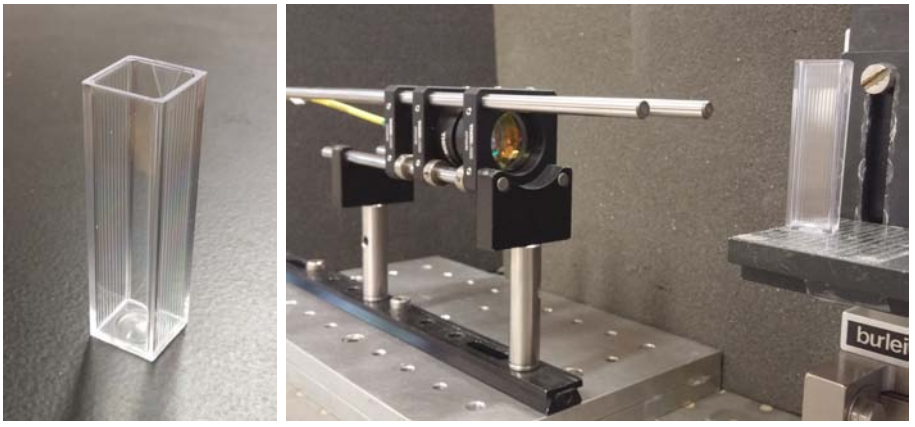

(a) Cuvette. (b) Position of the cuvette during the measurement.

Figure 5.2: Pictures of the container we used.

Figure 5.3 shows a preliminary A-Scan of an empty cuvette where we can identify its characteristic structure.

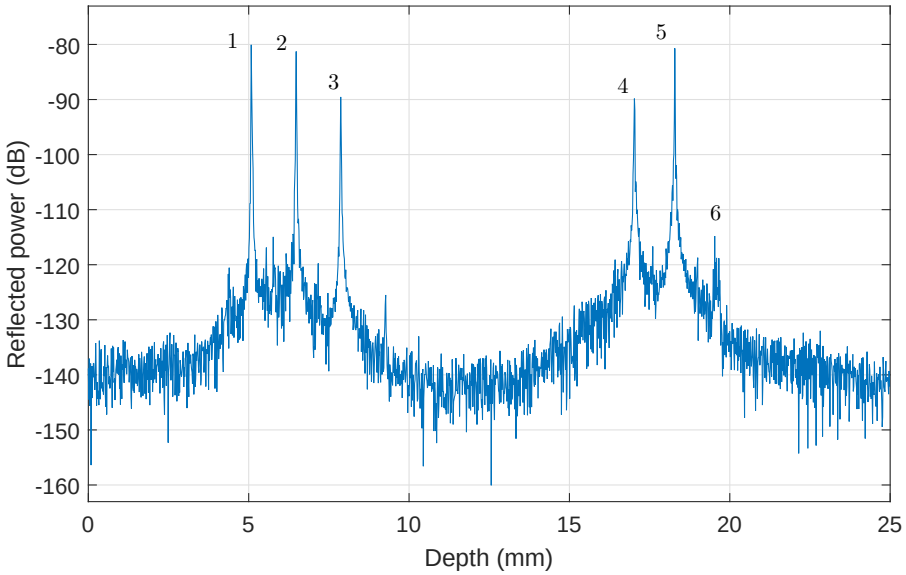

Figure 5.3: A-Scan of the cuvette.

Analysing the above trace, it is easy to see that the beam travelled through the entire sample. Four main reflection peaks can be highlighted and they represent the four interfaces of the cuvette:

- the first peak is the air/plastic interface on the external surface of the first wall;
- the second is the plastic/air interface on the internal surface of the same wall;
- the fourth and the fifth peak represent the second wall of the cuvette and its two interfaces.

In the above figure we can see other non-negligible peaks: they refer to multiple internal reflections inside the cuvette that show up in the analysis as fictitious interfaces. They disappear when the cuvette is not empty.
Then we proceeded to measure the distances between the peaks in order to see if they coincided with the actual physical dimensions, previously measured

Table 5.1: Cuvette: theoretical measures.

Parameter	**Value**
Wall depth	1 mm
Internal interspace width	10.5 mm
External width	12.5 mm

with a calibre and reported in Table 5.1. The distances obtained from the above trace had to be modified to account for the actual refraction index of the sample. As mentioned before, the refraction index we chose to use for the A-Scan is $n_{ref} = 1$, so in order to calculate the real distances we had to make use of equation 5.1:

$$\Delta z^{1,2} = \Delta z^{1,2}_{ref} \frac{n_{ref}}{n_{cuv}} \simeq 1.41 \frac{1}{1.35} \simeq 1.04\ mm,$$
$$\Delta z^{2,4} = \Delta z^{2,4}_{ref} \frac{n_{ref}}{n_{air}} \simeq 10.54 \frac{1}{1} = 10.54\ mm,$$
$$\Delta z^{4,5} = \Delta z^{4,5}_{ref} \frac{n_{ref}}{n_{cuv}} \simeq 1.40 \frac{1}{1.35} \simeq 1.03\ mm,$$
$$\Delta z^{tot} = \Delta z^{1,2} + \Delta z^{2,3} + \Delta z^{3,4} = 12.61\ mm,$$

where the value of the refraction index of the cuvette ($n_{cuv} = 1.35$) was determined in previous analyses of the trace obtained from the OBR. As we can see, the estimated distances are very similar to the theoretical ones.

After these preliminary measurements, we proceeded with the evaluation of a 2D portion of the cuvette. We positioned the container as in Figure 5.2 in order to scan either a vertical or a horizontal section of it. This is done by shifting the sample in the two directions with the help of the Burleigh translator (x and y-axis highlighted in Figure 4.6).

During the acquisition of the images we decided to rotate the base of the cuvette by a few degrees because we noticed that its walls cannot be positioned perpendicularly to the beam if we are to avoid a direct reflection that could saturate the detector and degrade the quality of the images.

Vertical scan

First, we made a vertical scan to identify the structure of the cuvette. From the analysis of the A-Scan in Figure 5.3 we expected an image with four vertical interfaces and other fictitious ones. We chose a transversal resolution of 50 μm, which is not the highest possible one, because the cuvette has a simple and regular structure that is easy to identify even with a lower resolution. Besides, by increasing the sampling step we reduced the number of A-Scans and the acquisition time. The parameters used for the scan are reported in Table 5.2.

Table 5.2: B-Scan: parameters.

Parameter	**Value**
n_{mis}	300
transversal resolution	50 μm
total length	15 mm
time of acquisition	$\sim$ 100 min

The resulting B-Scan is shown in Figure 5.4. From these results we can make some observations:

- the image is quite clear, the front and rear interfaces of the cuvette are clearly defined and easily identifiable;
- the shape in the figure matches the real structure of the sample: it is possible to apply the same correction of the refraction index we used before to obtain the real depth of the walls;
- as we expected there are fictitious interfaces due to multiple internal reflections.

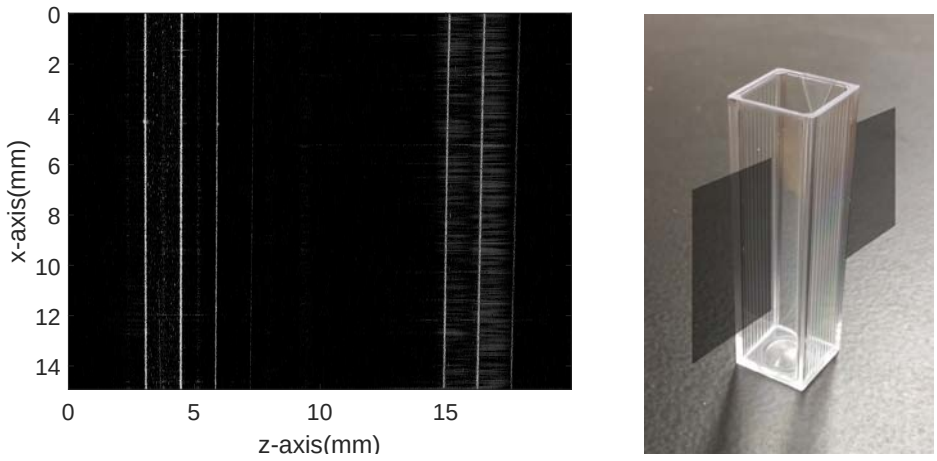

(a) Intensity image. (b) B-Scan section.

Figure 5.4: Veritcal B-Scan of the cuvette. Intensities are reported in logarithmic scale (dB).

Horizontal scan

We also made a horizontal scan in order to obtain a better image of its internal structure. The parameters used for the scan are the same as the previous ones (Table 5.2) and Figure 5.5 shows the B-Scan image obtained after the post-processing.

Analysing the figure we can make some considerations:

- the shape of the cuvette is easy to identify in the image and it matches its real structure. The rotation of the base and the presence of the walls of the container are clearly visible;
- the image is not totally clear because the measure is influenced by the internal reflections of the cuvette. These reflections, as explained before, lower the image contrast and generate fictitious interfaces;
- as we expected the upper and lower walls in figure are not well defined because the incident beam hits these interfaces at a large angle and only a small fraction of the light is reflected back to the fiber;
- the other two walls are clearly defined and it is possible to determine

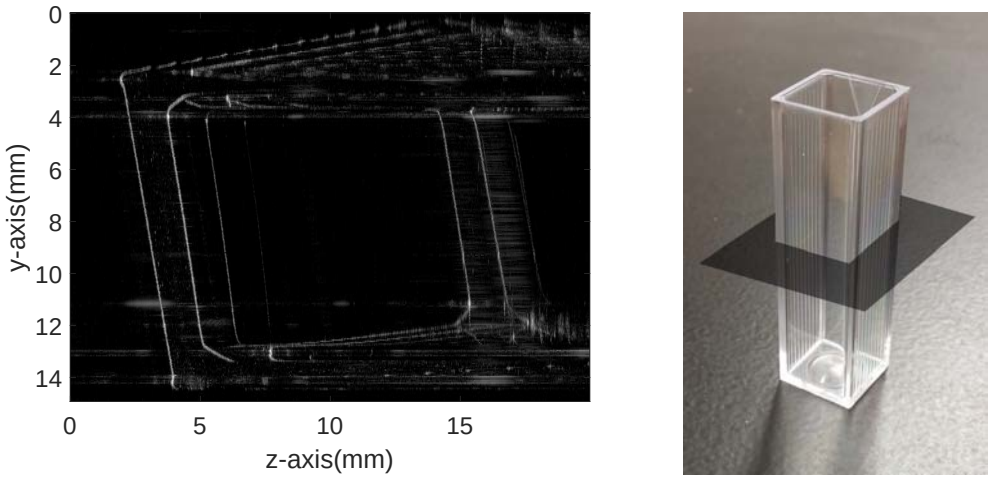

(a) Intensity image.

(b) B-Scan section.

Figure 5.5: Horizontal B-Scan of the cuvette. Intensities are reported in logarithmic scale (dB).

their depth and inclination. In particular, the wall on the left is clearer than the one on the right because the incident power on the first interface is higher and the resulting reflection bigger, since the light that reaches the back of the cuvette is the fraction of the radiation that remains after the first two reflections and the attenuation due to the plastic material.

5.1.3 Second sample: Adhesive tape

In this section we analyse a non-organic sample: a roll of adhesive tape. This material exhibits birefringence properties and it is used to study its effects on the polarization of the incident light. However this first setup was not capable of collecting enough information: the light hits the sample with a single arbitrary SOP, while at least two different SOPs are necessary to compute the birefringence. This particular study is presented later in the chapter.

The sample, as we can see in Figure 5.6, is a normal semi-transparent roll of adhesive tape, that can be easily purchased in a stationery shop. We placed

it on the support of the translator, in the position where the optical coupling between fiber and air is highest, the waist beam.

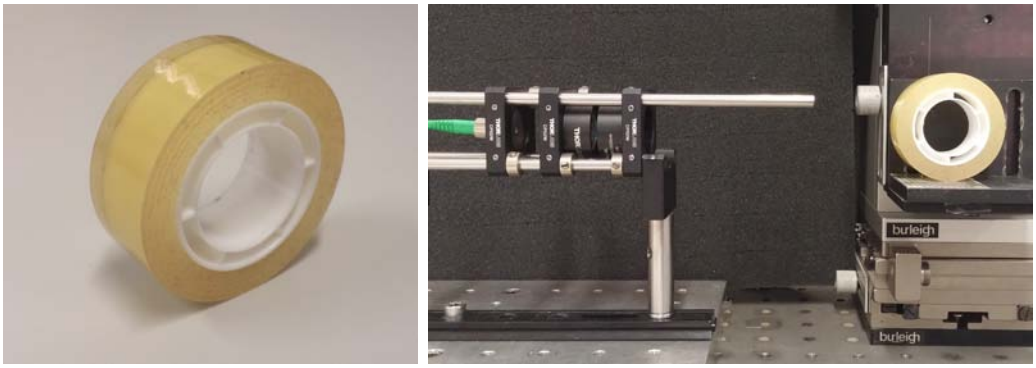

(a) Adhesive tape. (b) Position of the tape during the measurement.

Figure 5.6: Pictures of the roll of adhesive tape we used.

Analysis of the structure

With the help of this first setup we tried to identify the structure of the roll of tape by analysing the images obtained from multiple acquisitions. In Figure 5.7 we show how the sample was scanned and we highlight the section that was analysed. We generated an intensity image for each scan and we applied a threshold to increase the contrast of the figure. Specifically, all the values below the threshold are treated as background noise and displayed in black. That allows us to distinguish the edges of the tape, both the internal and the external one.

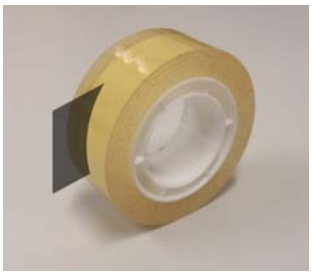

Figure 5.7: B-Scan section.

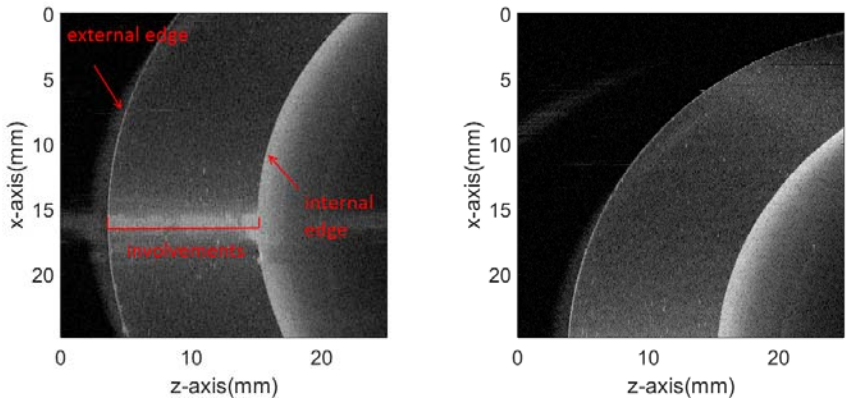

(a) Intensity image 1.

(b) Intensity image 2.

Figure 5.8: Vertical B-Scans of the roll of tape: transversal resolution = 100 μm, number of A-Scans = 250, acquisition time = $\sim$ 85 min. Intensities are shown in logarithmic scale (dB).

Figure 5.8 shows the results of two different B-Scans where the edges of the roll of tape are highlighted: the internal one is the interface between the tape and its internal support and as we can see it produces a high reflection, probably because of its low transmissivity. The geometry of the sample is not totally respected: it is accurate only up to the leftmost end of the layer of rolled tape (x = 16 mm in Figure 5.8(a)). To the right of it the roll appears to be deformed and stretched instead. This behaviour is easy to notice in Figure 5.8(b) where the sample has been scanned from the middle to the top and we can easily see that the coils of tape seem to thin near the top, which is of course not the shape of the real object.

Analysis of the behaviour of polarization

We can also use this system to study the behaviour of polarized light and its interaction with the sample. As mentioned before, the tape has birefringence properties and it can alter the polarization of the light that goes through it. We can measure with the OBR the x and y components of the electric field of the backscattered signal generated by the single arbitrary SOP that hits the sample. From these two components we computed the

Stokes vector for each point of the B-Scan as explained in section 2.4.1). Dividing it by its first component (S_0) we obtained its normalized form and plotted it to analyse the behaviour of the polarization of the light.
Figure 5.9 shows a zoom of the B-Scan obtained from the vertical scan of Figure 5.7. We processed the images so obtained and we again used a threshold to remove the background noise and increase the contrast. We then estimated the position of the edge, in order to create a reference for successive analyses. This estimation is based on the Canny's multistage algorithm: it first applies a Gaussian filter to smooth the image in order to remove the noise, then it locates potential edges by analysing the intensity gradients and finally it suppresses all edges that are weak and not connected to strongest ones. The result is the yellow line shown in the figure below.

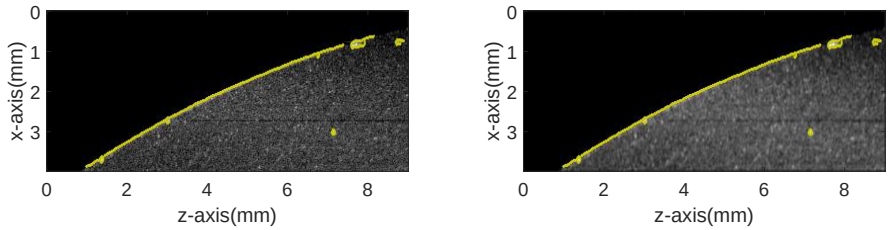

(a) B-Scan intensity image. (b) Smoothed B-Scan image.

Figure 5.9: Detail of a vertical B-Scan of the roll of tape. Intensities are shown in logarithmic scale (dB).

Figure 5.10 shows the components of the normalized Stokes vector after smoothing is applied: we filtered each single component and it is possible to identify the interaction between the tape and the polarized light. If we consider the section of the images outlined by the previously identified edge, we can notice a pattern in the way the components of the vector change. This common variation represents a change of polarization of the beam. Thin lines of different colours are visible in all images, each of them representing a particular state of polarization of the light that changes after every single coil of tape.
It is possible to verify the reliability of this analysis by considering the Degree of Polarization (DOP) of the light inside the tape. The DOP is estimated

using the smoothed versions of the Stokes components as the fraction of the total power that is carried by the polarised component of the wave and in particular:

$$DOP = \frac{\sqrt{S_1^2 + S_2^2 + S_3^2}}{S_0} \leq 1. \tag{5.2}$$

A perfectly polarized wave has a DOP equal to 1, whereas a wave with no polarization at all has a DOP of 0. A wave which is partially polarized, and therefore can be represented by a superposition of a polarized and a non-polarized component, will have a DOP between 0 and 1.

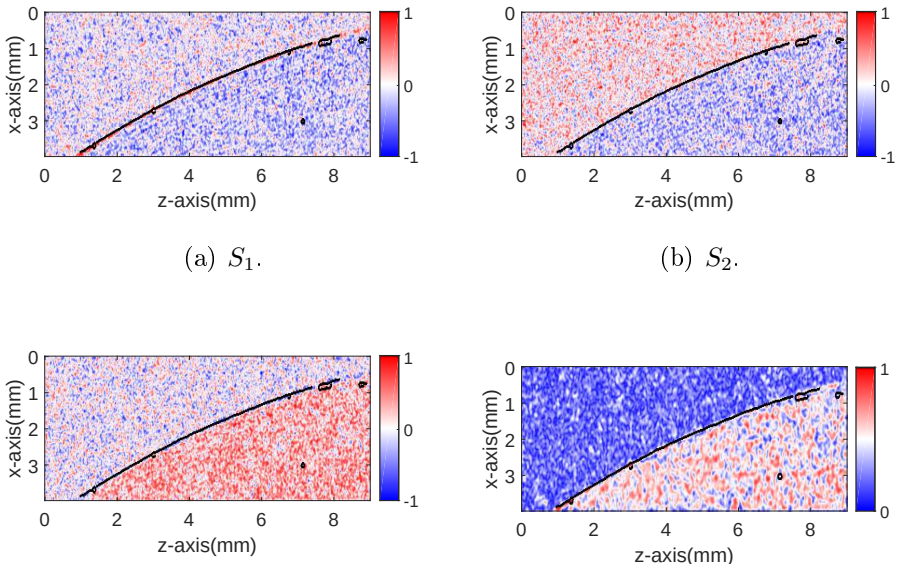

(a) S_1. (b) S_2.

(c) S_3. (d) DOP.

Figure 5.10: Components of the normalized Stokes vector and Degree of Polarization.

The DOP map shows that the beam is highly polarized inside the coils of tape. Therefore the information carried by the Stokes components is reliable.

As previously explained, the Stokes components can be used to identify a particular SOP on the Poincaré sphere. Figure 5.11 shows a graphical representation of the Stokes vector where the components are represented by the colour channels in an RGB image. We can see how the information we

have about the light beam inside the tape allows us to study the changes in polarization as the radiation goes deeper inside the sample. The figure also displays the same thin parallel lines corresponding to each single coil of tape, while the aleatory polarization changes observed outside the sample are not reliable due to the low degree of polarization in this region.

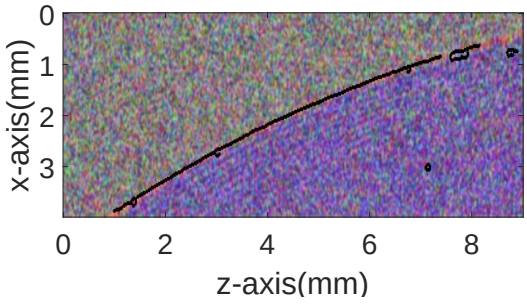

Figure 5.11: Graphical representation of the Stokes vector.

5.1.4 Characterization of the suspension

In the next sections a small Zebrafish sample is analysed with the second setup we implemented. Before proceeding to perform these tests we made some preliminaries analyses to characterize the suspension in which these samples are immersed.

Biologists usually use agarose as a gelling agent in order to make gel plates or overlays for cells in tissue culture. We exploited its features to create a suspension that is able to fix our organic sample in a stable position necessary to obtain a B-Scan image. We prepared with the help of Prof. Tiso some cuvettes filled with different concentrations of agarose: our aim was to analyse the different interaction between light and agarose for each sample we made.

The agarose we used is produced by SIGMA (product code A9414) and it is characterized by low gelling temperature. We dissolved the agarose powder in water with different concentration: 0.1%, 0.5%, 1% and 2%. In addition to that we prepared another suspension, a resin, in order to compare the agarose to other substances.

We scanned all these samples with our SS-OCT system and we obtained several vertical B-Scans, similar to the one obtained in Figure 5.4, but with a few differences:

- a higher reflected power inside the cuvette due to the presence of agarose;
- the lack of the two vertical lines representing the second wall. We suppose the light reflected from this interfaces is entirely absorbed by the suspension.

We are not going to present the images obtained from these scans because of their poor quality but we will exploit these data to study the absorption and scattering properties of the agarose and the resin, instead. Figure 5.12 shows the comparison between the different percentages of agarose and the resin. All images were obtained by computing the average of the backscattered intensities along the vertical direction for each point of the B-Scan z-axis. As a result, we obtain the average horizontal A-Scans shown in the figure.

From these analyses we can extract the desired information about absorption. The figure shows the normalized A-Scans obtained by dividing - on a linear scale - each point by the maximum backscattered intensity measured at the detector which corresponds to the power reflected by the first wall of the cuvette. The intensities shown are then represented in logarithmic scale for a better estimation of the losses caused by the material under examination. This logarithmic and normalized form allows us to compare the different concentrations of agarose and the resin. So we can evaluate:

- the fraction of the light that the substance retroreflects by analysing the intensity of the backscattered radiation just after the peak related to the second interface of first wall;
- the absorption of the substance by linear interpolation of the curve that represents the intensity of the backscattered light inside the cuvette.

For this purpose, we focused on a portion of the graphs shown in Figure 5.12. We considered the downward sloping part of the curve that goes from right after the second peak up to the position where the intensity is almost equal

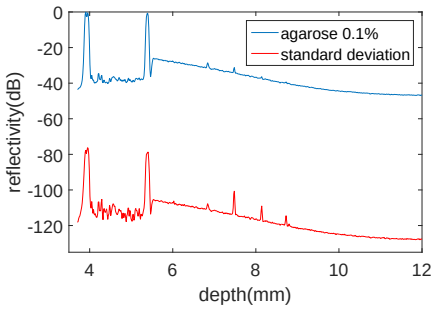

(a) Agarose 0.1%.

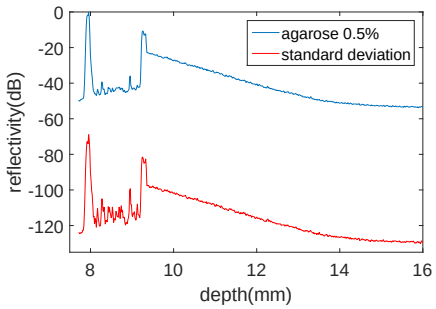

(b) Agarose 0.5%.

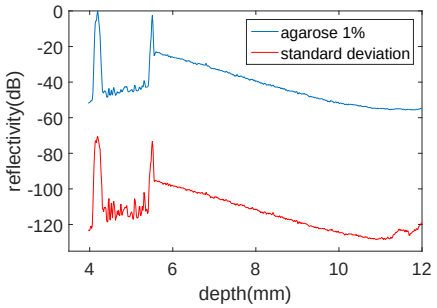

(c) Agarose 1%.

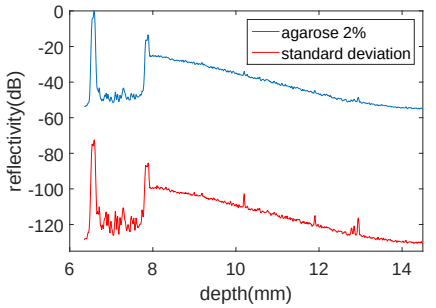

(d) Agarose 2%.

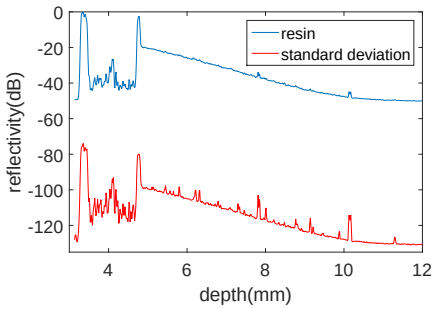

(e) Resin.

Figure 5.12: Average A-Scans of the suspensions.

to the background noise. Then we linearly interpolated the selected data in order to obtain the absorption coefficient of the suspension.

We can verify that our analysis is reliable by evaluating the standard deviation of the previously computed average that we reported in Figure 5.12. As we can see, the error in the portion of the A-Scan we considered is very low

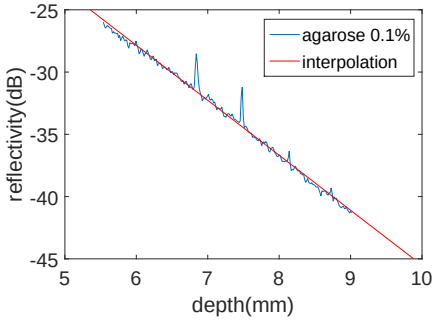

(a) Agarose 0.1%.

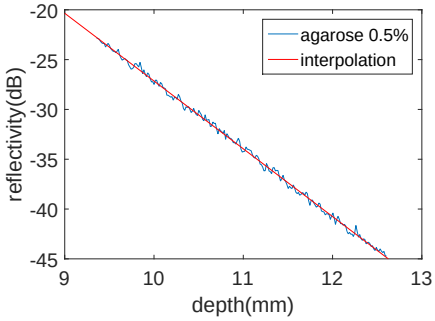

(b) Agarose 0.5%.

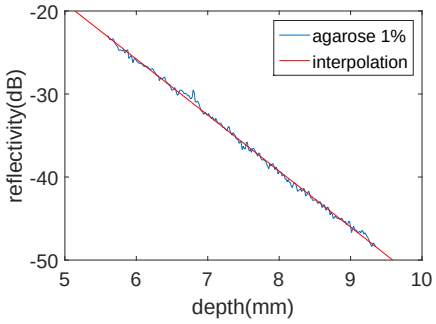

(c) Agarose 1%.

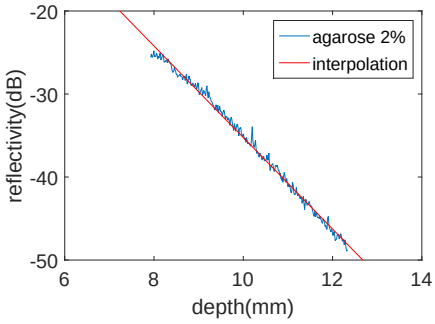

(d) Agarose 2%.

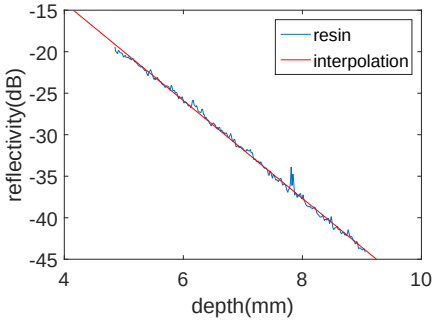

(e) Resin.

Figure 5.13: Absorption curves.

and this supports our thesis. We show the absorption curves and their linear interpolation in Figure 5.13.

The absorption coefficients we computed and the value of the backscattered light we measured at the cuvette/suspension interface are shown in Table

5.3.

Table 5.3: Absorption coefficients.

Substance	**Absorption coefficient**	**Backscattered light**
Agarose 0.1%	-4.42 [dB/mm]	-25.98 dB
Agarose 0.5%	-6.80 [dB/mm]	-22.83 dB
Agarose 1%	-6.74 [dB/mm]	-23.00 dB
Agarose 2%	-5.51 [dB/mm]	-25.60 dB
Resin	-5.89 [dB/mm]	-19.41 dB

Those absorption coefficients show how the backscattered light is attenuated by the agarose or the resin. If we suppose the substance to be homogeneous, we can assume that the fraction of light that is retroreflected is the same at each point along the longitudinal axis. As we go deeper into the substance what changes is the remaining total intensity after these multiple reflections. A high reflectivity encountered after the cuvette/suspension interface means that a high fraction of the light is retroreflected at each point. Furthermore, a high absorption coefficient reduces the depth of focus.
In order to obtain the highest possible quality in our images of the Zebrafish sample, we identified as most suitable for our needs the agarose with a concentration of 0.1%: it's the one that has the lowest absorption coefficient and that minimizes the amount of backscattered light among the various samples we analysed.

There is a trend in the reflectivity data that is worth pointing out. We expected a higher absorption rate as the concentration of agarose increased, but the actual values didn't match our expectations: when the concentration of agarose was higher than 1%, the absorption and reflectivity we measured were lower than they were in the 0.5% case, although they were still higher than the ones obtained with the 0.1% solution.
Future work should further investigate this behaviour and analyse higher concentrations of agarose to completely characterize its absorption and re-

flectivity properties.

5.2 Polarization sensitive SS-OCT

5.2.1 First sample: roll of tape

We tested the system on the same roll of tape used before in order to study in detail the birefringence of the material. Our setup can measure two different SOPs as explained in section 4.2.2 and use them to compute the birefringence of the sample. As in previous scans, we positioned the sample in the "waist beam" to obtain a high coupling between fiber optic and air, the best possible resolution and the highest focus depth. Then we proceeded to make a horizontal scan as in Figure 5.14. It was composed of 1300 different A-Scans with a transversal resolution of 15 μm. The resulting total shift of the sample was about 1.95 cm and the entire process took 8 hours to complete.

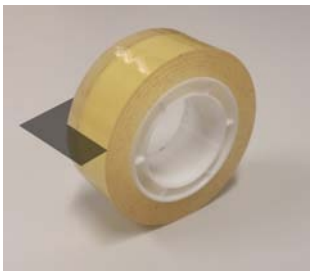

Figure 5.14: B-Scan section.

We processed the data so obtained and created an intensity image of the received signal, shown in Figure 5.15(a), where we applied a threshold to reduce the overall noise generated by the external environment. We can identify from the figure the structure of the reel, similar to what we saw in the previous section: a first edge - highlighted in yellow - represents the air/tape interface, the second one corresponds to the internal reel and presents a high reflection, identified by the white band. Figure 5.15(b) shows a close-up of the section inside the red rectangle that will be used in the following analyses to better evaluate the behaviour of polarized light for both SOPs.

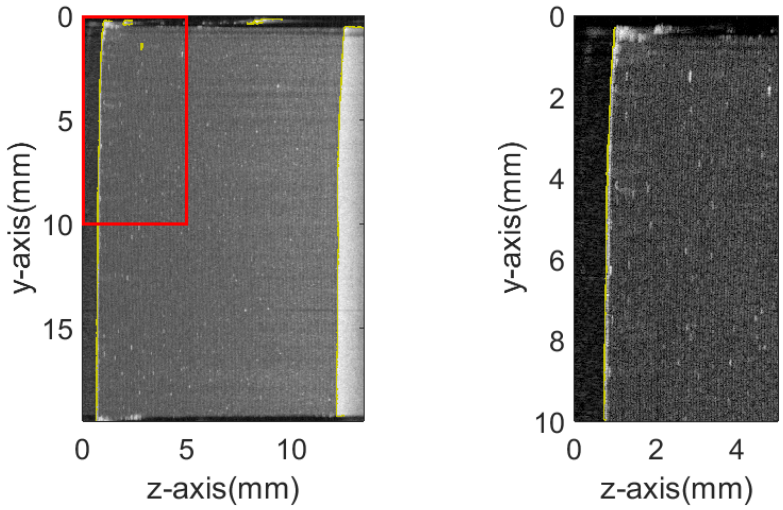

(a) Smoothed B-Scan image. (b) Zoom of the B-Scan.

Figure 5.15: Horizontal B-Scan. The magnified area is highlighted in red.

This system is also able to detect the state of polarization of the light for both signals received at the detector so we computed the two Stokes vectors for each point of the image. Their normalized form is plotted in Figure 5.16 and 5.17. From the figures, we can see how the components vary in an even and regular way inside the tape, just like we saw in the previous analysis. Comparing Figure 5.16 and 5.17 we can see the non-orthogonality of the two SOPs used to scan the sample - as we expected from the use of the beam splitters and the subsequent manipulations described in a previous chapter. The components of the Stokes vector of the first SOP are characterized by a predominant blue colour (which represent values around -1). In the second case the dominant color is red (values near 1) for the first two components, while the third one is similar to the corresponding component of the first SOP instead. That means that their positions on the Poincaré sphere are not parallel, and therefore the two states of polarization are not orthogonal. This analysis is confirmed by the evaluation of the degree of polarization inside the tape: Figure 5.18 shows the DOP for each SOP and how light is highly polarized inside the tape but not outside it. We can also see that light is not polarized near the top edge of the image, while on the left of the black

edge the behaviour of the DOP is not regular probably due to undesired reflections on the surface of the tape.

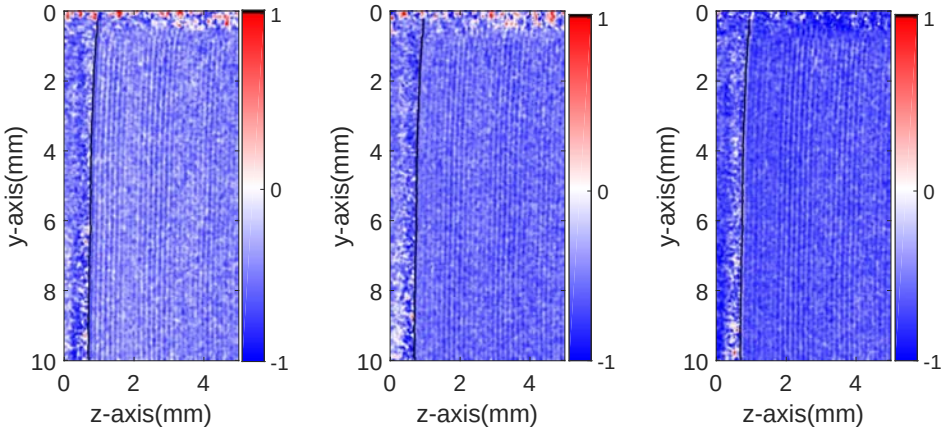

(a) S_1. (b) S_2. (c) S_3.

Figure 5.16: Components of the Normalized Stokes vector for SOP1.

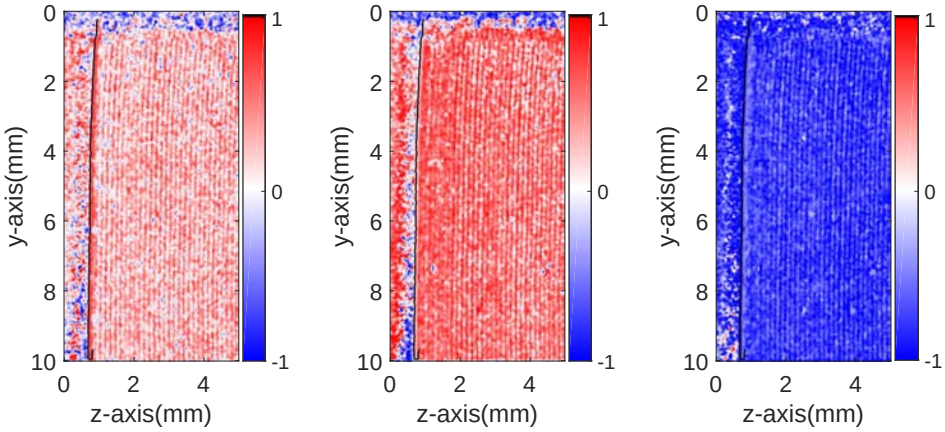

(a) S_1. (b) S_2. (c) S_3.

Figure 5.17: Components of the Normalized Stokes vector for SOP2.

Figure 5.19 shows the behaviour of each SOP on the Poincaré sphere. We present a graphical representation of the Stokes vector whose component are again encoded in the three colour channels in an RGB image. Here too we

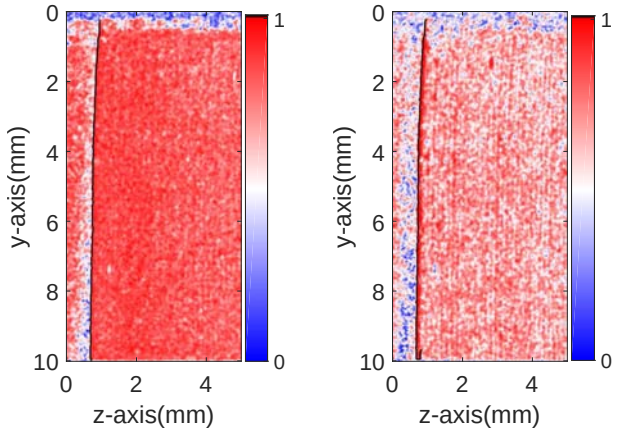

(a) DOP for SOP1. (b) DOP for SOP2.

Figure 5.18: Degree of Polarization of the light for the two SOPs.

can see the same thin parallel lines corresponding to each coil of tape, while outside the sample the polarization changes randomly. We highlight that the colours of two SOPs in the figure are relative to non-opposite vectors on the Poincaré sphere and consequently non-orthogonal polarizations.

Now we can proceed with the computation of the birefringence of the sample. First, we implemented an algorithm based on [21] to compute the vector $\bar{v}_R$ that is proportional to the Polarization Mode Dispersion (PMD) vector Ω and to the roundtrip birefringence vector. In particular we have

$$\bar{v}_R = \bar{\Omega} \cdot df = \bar{\beta}_R \cdot dz. \tag{5.3}$$

This algorithm exploits the evolutions of the Stokes vectors of at least two different SOPs as a function of depth in order to compute $\bar{v}_R$, the rotation vector. It is necessary to divide it by the sampling step dz to obtain the roundtrip birefringence vector $\bar{\beta}_R$. The modulus of this vector represents the birefringence information as already shown in equation equation 3.21

$$|\bar{\beta}_R(z)| = 2|\bar{\beta}_L(z)|,$$

where we assume $\eta \simeq 0$. So, we can write the desired birefringence information as

$$|\bar{\beta}| \equiv |\bar{\beta}_L| = \frac{|\bar{\beta}_R|}{2} \quad \left[\frac{rad}{m}\right]. \tag{5.4}$$

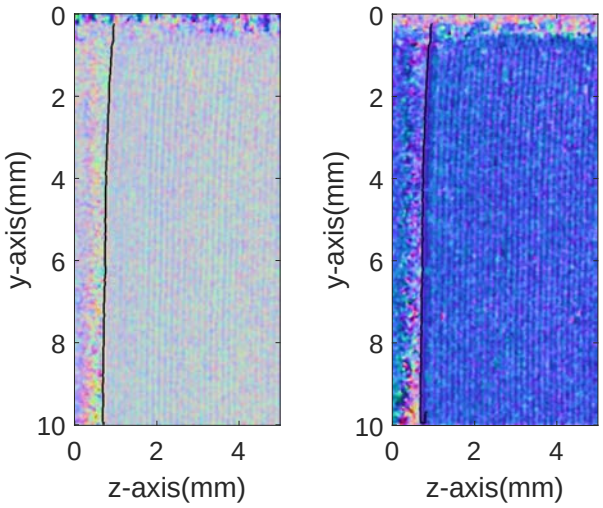

(a) SOP1. (b) SOP2.

Figure 5.19: Graphical representation of the Stokes vector.

The birefringence image we obtained is shown in Figure 5.20(a). As we can see, the birefringence inside the sample is quite homogeneous but difficult to evaluate due to the wide range of values. We can estimate its value by averaging along the *y-axis*, and the result is shown in Figure 5.20(b), where the red line shows the average value, which is equal to $4.85 \cdot 10^3 \ \frac{rad}{m}$. That corresponds to $4.85 \ \frac{rad}{mm}$ and a full oscillation every $2\pi/4.8 \simeq 1.3$ mm. We noticed high values of birefringence outside the white edge in the image, but here the light is only minimally polarized (see Figure 5.18) and the information we have is not reliable.

5.2.2 Second sample: Zebrafish

In our final measurements we used a biological sample: a specimen of *Brachydanio rerio* of about $1mpf$ (month post fertilization), commonly known as Zebra "Danio" or Zebrafish. This sample were prepared by Prof. Natascia Tiso, according to the authorization CEASA - project 407/2015-PR - of the University of Padova. The specimen was anaesthetized and euthanized with the use of tricaine (SIGMA A5040) that was dissolved in distilled water with

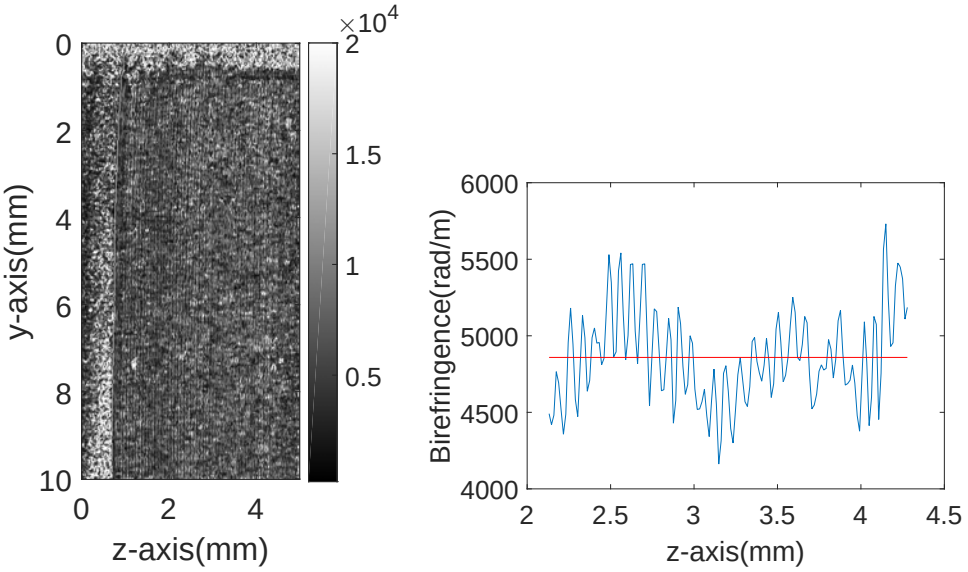

(a) Tape birefringence image. (b) Value of birefringence inside the sample.

Figure 5.20: Birefringence of the adhesive tape.

a concentration of 0.3 mg/ml. The sample was subsequently immersed for one night in a 4% PFA (paraformaldehyde - SIGMA P6148) solution in PBS (phosphate-buffered saline - SIGMA P4417) in order to fix the tissues and to slow down the decomposition process. The Zebrafish was finally immersed in agarose previously dissolved in distilled water with a concentration of 0.1% as we decided after the analyses described in section 5.1.4. The sample is shown in Figure 5.21.

We will now analyse three coronal sections of the sample and two transversal ones in order to identify all the parts and anatomical components of the specimen. We took three different coronal sections because of the particular position of the sample. As we can see in the above picture, the sample was not positioned correctly along the longitudinal axis, so we had to repeat the measurement in different positions.

Coronal section 1

We scanned the lower coronal section of the sample as shown in Figure 5.22 in order to hit the the head and the abdomen of the Zebrafish. The

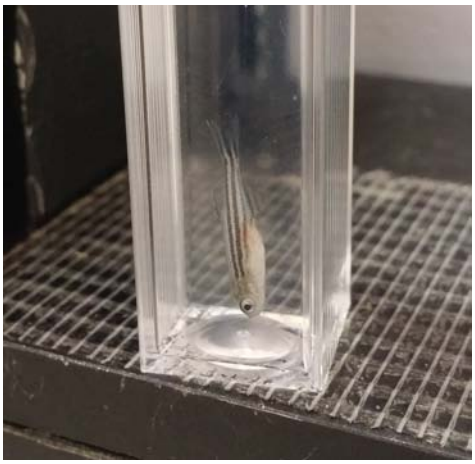

Figure 5.21: Picture of the biological sample.

parameters of the B-Scan are reported in Table 5.4.

Figure 5.22: B-Scan section.

Figure 5.23(a) shows the intensity (in logarithmic scale) of the B-Scan and the anatomical analysis Prof. Tiso did. Figure 5.23 reports the estimation of the shape we made with the Canny algorithm. We applied an intensity threshold to reduce the background noise and increase the contrast of the image. We can see that the scan is incomplete and its right side is missing. That's because the tissues of the sample are rich of water, in particular the abdomen and the eye, and that increases the absorption of light.

In Figure 5.24 and Figure 5.25 we report the images of each component of Stokes vector for both the SOPs and we can see how this section of the biological sample doesn't affect the polarization of the light: it is possible to identify some polarization changes within the sample but they are probably not caused by interactions between light and muscle fibers.

Figure 5.26 shows the graphical representation of the Stokes vector on

Table 5.4: B-Scan: parameters.

Parameter	**Value**
n_{mis}	668
transversal resolution	15 μm
total length	10 mm
time of acquisition	$\sim$ 4 h 15 min

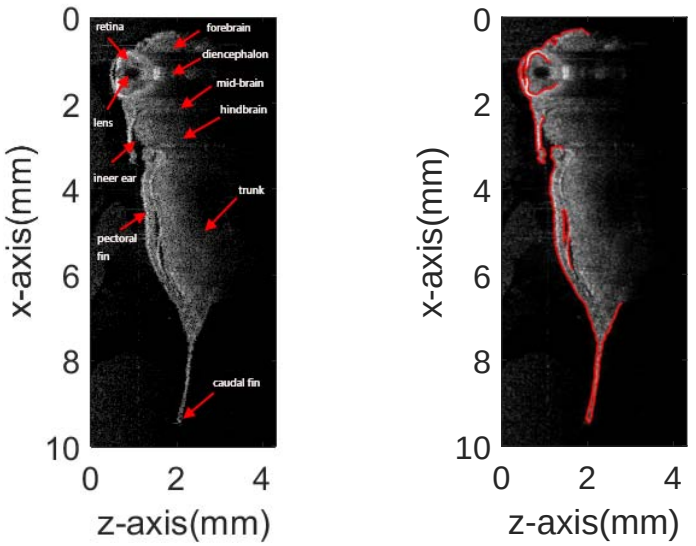

(a) B-Scan image (SOP1). (b) Edge estimation.

Figure 5.23: Vertical B-Scan.

the Poincaré sphere. These images show how the polarization doesn't change significantly within the area bounded by the edge. The polarization data we have is reliable due to the high degree of polarization inside the sample as we can see in Figure 5.27. It is also possible to identify the presence of a small portion of the tail and a change of polarization when light passes through the pectoral fin.

The birefringence image in Figure 5.28 shows the areas where the degree

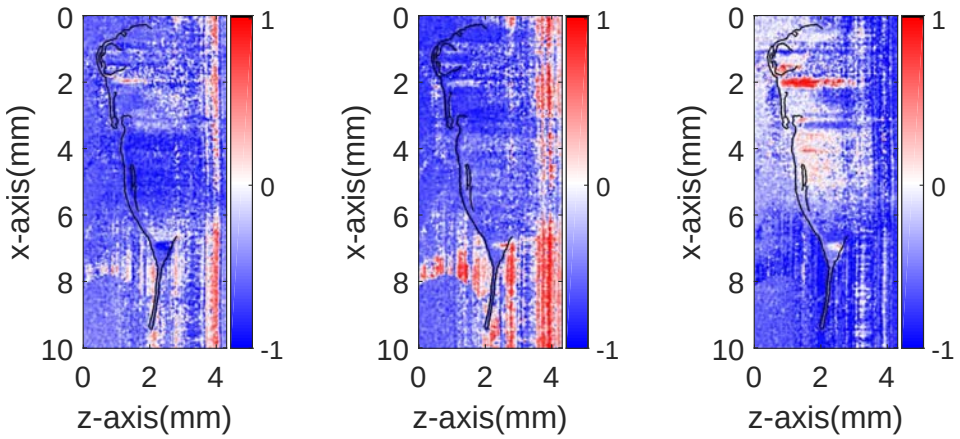

(a) S_1. (b) S_2. (c) S_3.

Figure 5.24: Components of the Normalized Stokes vector for SOP1.

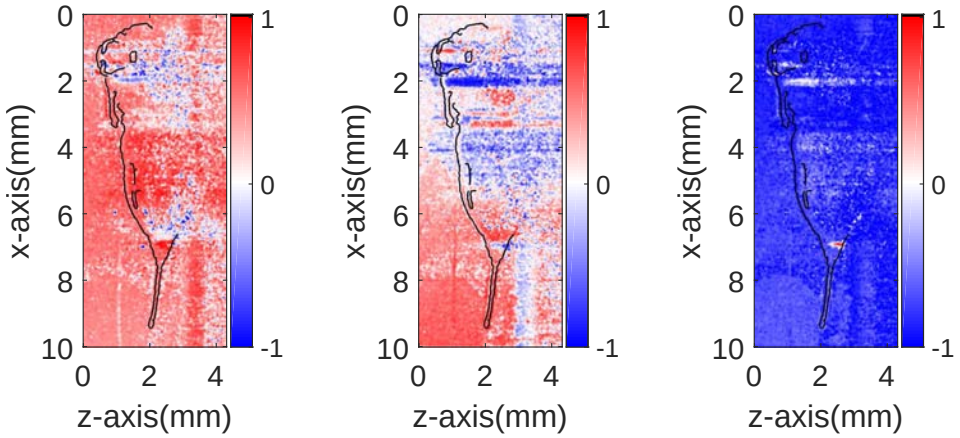

(a) S_1. (b) S_2. (c) S_3.

Figure 5.25: Components of the Normalized Stokes vector for SOP2.

of polarization is almost equal to 1 and polarization changes are birefringent, such as the small portion of the tail. We cannot evaluate the behaviour of birefringence in the rest of the sample because light there is not very polarized. Also the high values we can see outside the edge are not reliable.

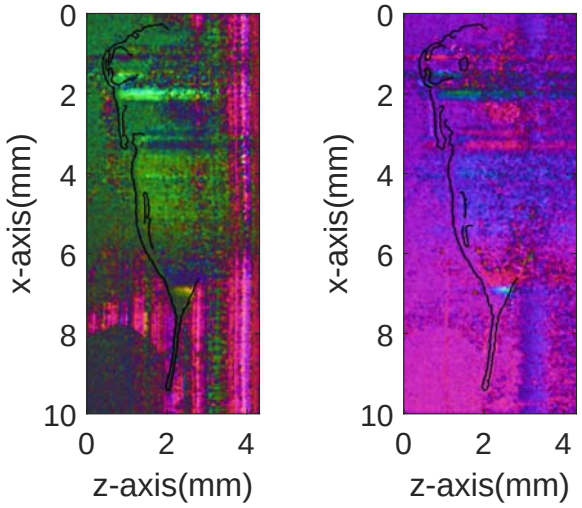

(a) SOP1. (b) SOP2.

Figure 5.26: Graphical representation of the Stokes vector.

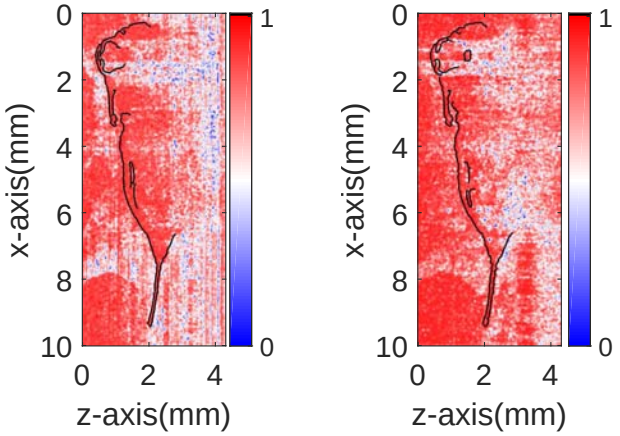

(a) DOP for SOP1. (b) DOP for SOP2.

Figure 5.27: Degree of Polarization of the light for the two SOPs.

Coronal section 2

The scan shown in Figure 5.29 includes a larger section of the tail muscle and some internal organs of the Zebrafish. The parameters of the B-Scan are reported in Table 5.5.

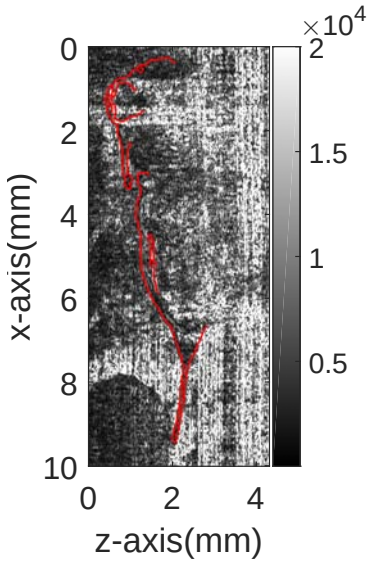

Figure 5.28: Birefringence image of coronal section 1 of the Zebrafish.

Figure 5.29: B-Scan section.

Figure 5.30(a) shows the intensity (on a logarithmic scale) of the B-Scan and the anatomic analysis of Prof. Tiso. Figure 5.30 reports the estimation of the shape we made with the Canny algorithm. We applied an intensity threshold to remove lower background noise and to increase the contrast of the image. As we can see, this scan intersected the brain of the fish, the swim bladder and a large portion of the tail. The image is clearly defined here because the concentration of water is smaller and so is the absorption of light, and the result is a higher depth of focus.

Figure 5.31 and 5.32 show the images of each component of Stokes vector for both SOPs and we can easily see how the muscles of the tail affect the polarization of the light: it is possible to identify the central area of the tail where the polarization changes as it travels down the z-axis. There are also

Table 5.5: B-Scan: parameters.

Parameter	**Value**
n_{mis}	948
transversal resolution	15 μm
total length	14.2 mm
time of acquisition	$\sim$ 5 h 57 min

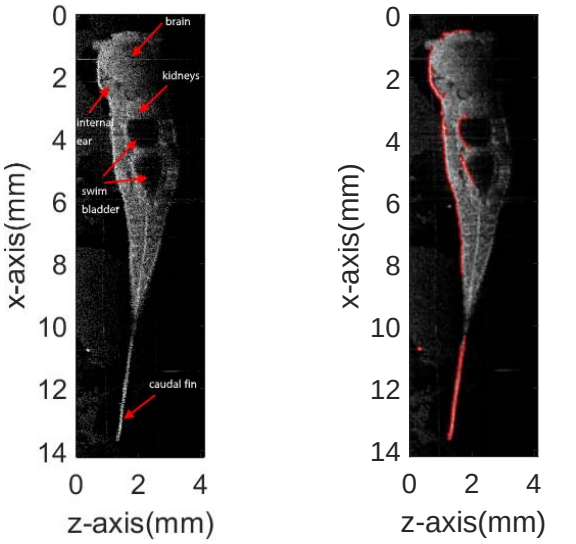

(a) B-Scan image (SOP1).

(b) Edge estimation.

Figure 5.30: Vertical B-Scan.

other areas where polarization changes such as the left and right external side of the body.

Figure 5.33 shows the graphical representation of the Stokes vector on the Poincaré sphere and the behaviour of its three components. In particular, polarization changes within the area of the tail.

We also report the analysis of the degree of polarization in Figure 5.34. It

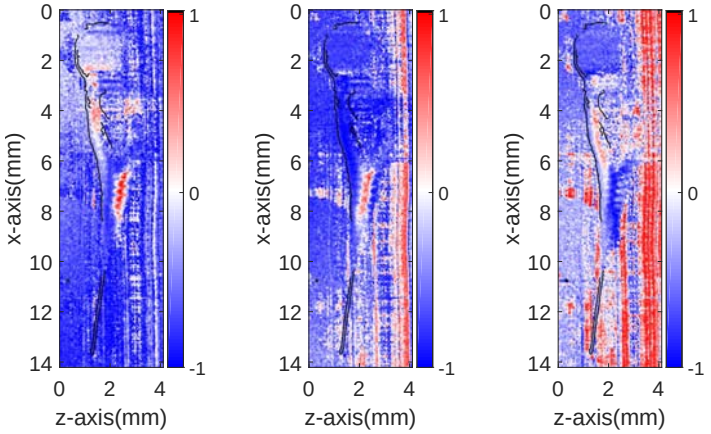

(a) S_1. (b) S_2. (c) S_3.

Figure 5.31: Components of the Normalized Stokes vector for SOP1.

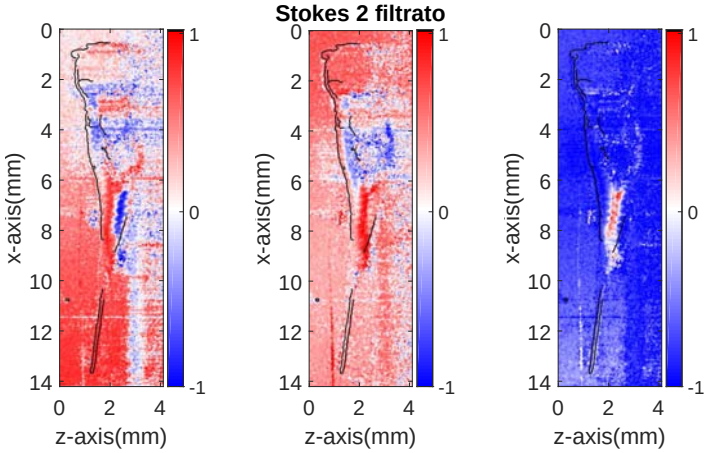

(a) S_1. (b) S_2. (c) S_3.

Figure 5.32: Components of the Normalized Stokes vector for SOP2.

confirms the observation we made above because the light is polarized within the tail area and in the left portion of the sample.

The birefringence image in Figure 5.35 shows how the tail muscles we highlighted before exhibit birefringence properties. Here the value of birefringence is higher than in the left area of the shape. We cannot estimate the behaviour of birefringence in the central part of the sample where the

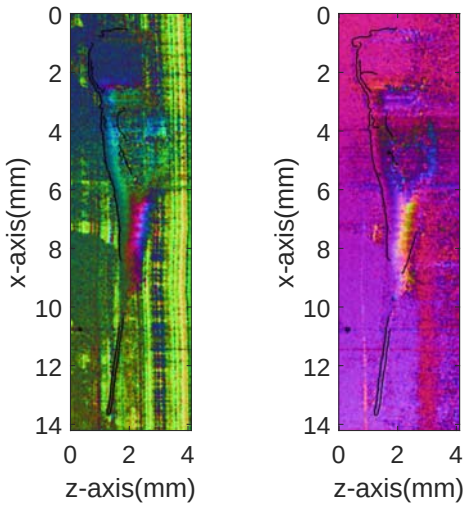

(a) SOP1. (b) SOP2.

Figure 5.33: Graphical representation of the Stokes vector.

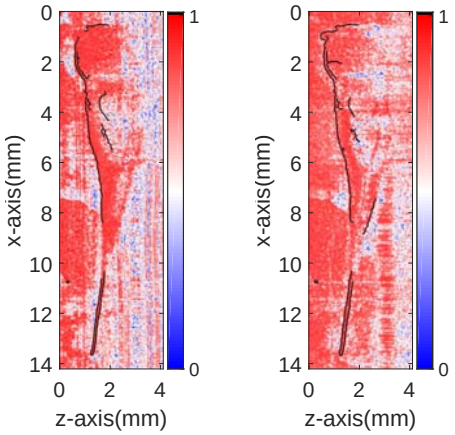

(a) DOP for SOP1. (b) DOP for SOP2.

Figure 5.34: Degree of Polarization of the light for the two SOPs.

swim bladder is and light is not quite polarized. This is probably due to the presence of other tissues that are not birefringent. The high values we can see outside the red edge are not reliable due to the low degree of light polarization and their lack of significance in our analysis.

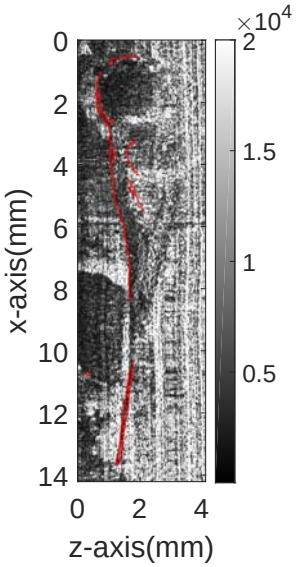

Figure 5.35: Birefringence image of coronal section 2 of the Zebrafish.

Coronal section 3

We chose to scan also the upper coronal section of the sample as shown in Figure 5.36 in order to scan the tail muscle and a portion of the head of the Zebrafish. Table 5.6 list the parameters of the B-Scan.

Figure 5.36: B-Scan section.

Figure 5.37(a) shows the B-Scan intensities on a logarithmic scale and the edge estimation made with the Canny algorithm is presented in Figure 5.37. We will use it in the next analyses to mark the shape of the sample. We also applied an intensity threshold to increase the quality of the image by removing lower background noise. Figure 5.37(a) also shows the Prof. Tiso's anatomical analysis.

Figure 5.38 and Figure 5.39 show the images of each component of Stokes vector for both SOPs and we can easily see how the muscles of the tail affect

Table 5.6: B-Scan: parameters.

Parameter	**Value**
n_{mis}	927
transversal resolution	15 μm
total length	13.9 mm
time of acquisition	$\sim$ 5 h 48 min

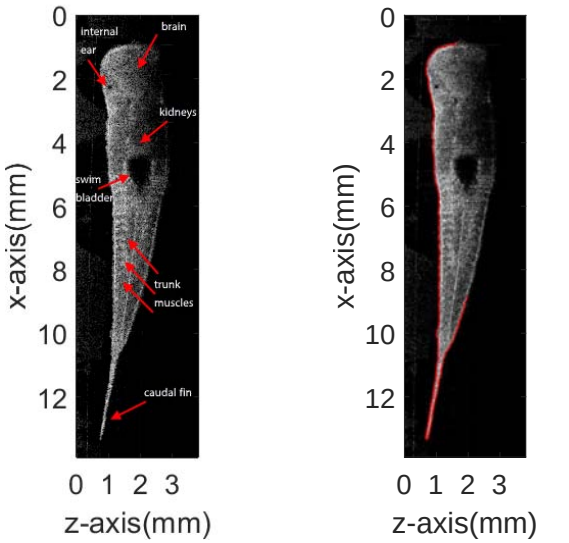

(a) B-Scan image (SOP1).

(b) Edge estimation.

Figure 5.37: Vertical B-Scan.

the polarization of the light: it is possible to identify the central area of the tail where the polarization changes as the light passes through the sample along the z-axis.

We show in Figure 5.40 the graphical representation of the Stokes vector on the Poincaré sphere. These images sum up the behaviour of the three components we seen above and the polarization appears to change within

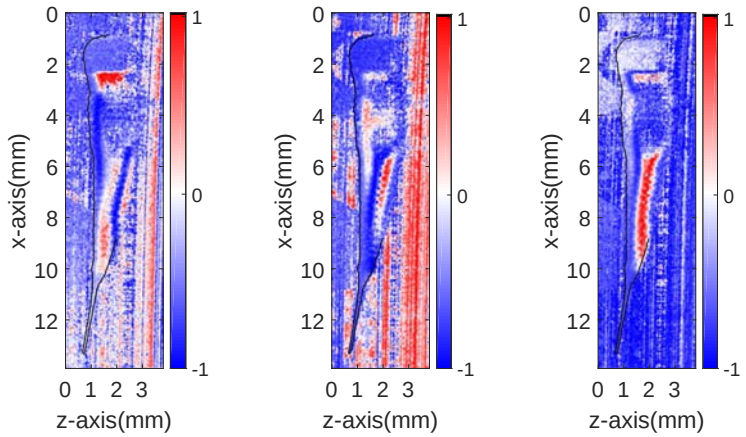

(a) S_1. (b) S_2. (c) S_3.

Figure 5.38: Components of the Normalized Stokes vector for SOP1.

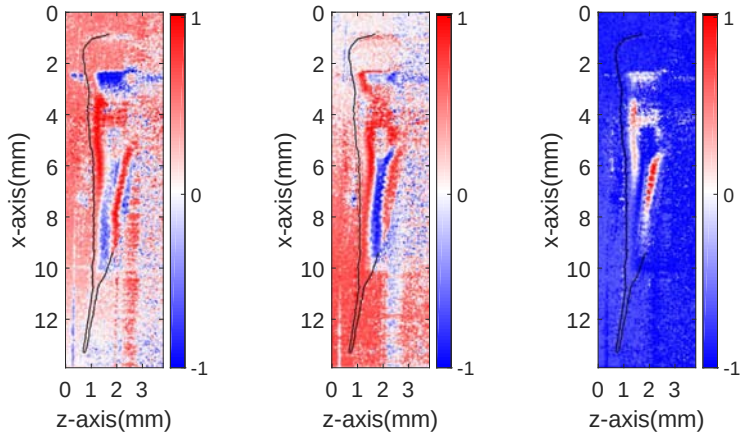

(a) S_1. (b) S_2. (c) S_3.

Figure 5.39: Components of the Normalized Stokes vector for SOP2.

the sample, in particular in the area of the tail.

We also report the analysis of the degree of polarization: as we can see in Figure 5.41 the light is polarized within the sample and this suggest that the observations we made before are reliable.

The birefringence image in Figure 5.42 shows how the tail of the sample and more specifically the muscles inside it exhibit birefringence properties.

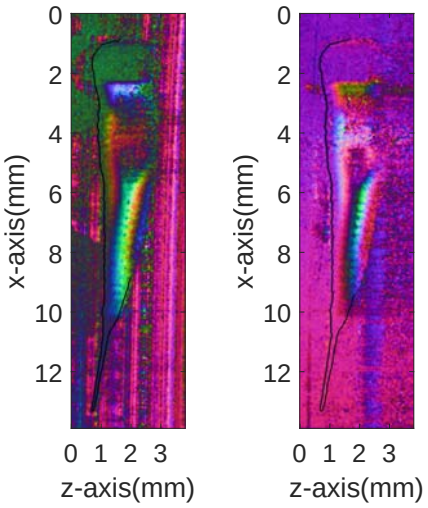

(a) SOP1. (b) SOP2.

Figure 5.40: Graphical representation of the Stokes vector.

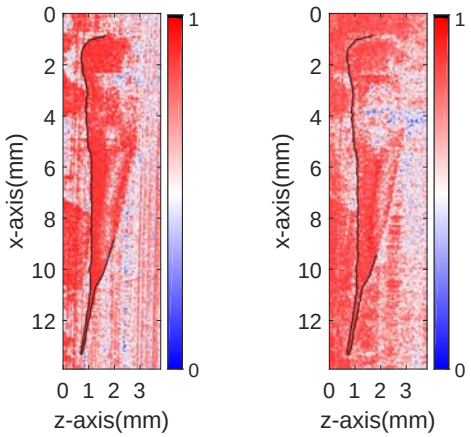

(a) DOP for SOP1. (b) DOP for SOP2.

Figure 5.41: Degree of Polarization of the light for the two SOPs.

In the specific area in which polarization appears to change in Figure 5.40 the birefringence is higher than in the rest of the tail as we expected. Within the rest of the tail the value of birefringence is quite homogeneous, and this is also true in the upper area of the shape. We can not evaluate the behaviour

of birefringence in the central part of the sample where the light is not quite polarized. This is probably due to the presence of other tissues that are not birefringent. The high values we can see outside the edge are not reliable and are not relevant for our analysis.

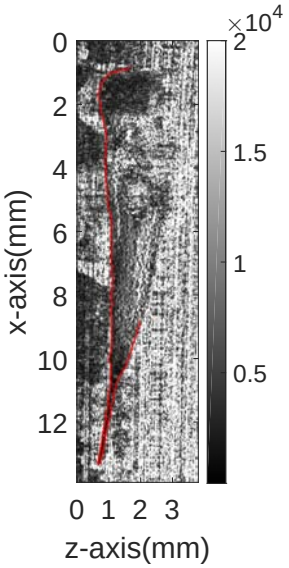

Figure 5.42: Birefringence image of coronal section 3 of the Zebrafish.

Transversal section 1

Figure 5.43 shows a scan of the tail of the fish whose parameters are listed in Table 5.7: we chose this particular section because the tail is composed of muscle fibers that are birefringent as mentioned in section 1.

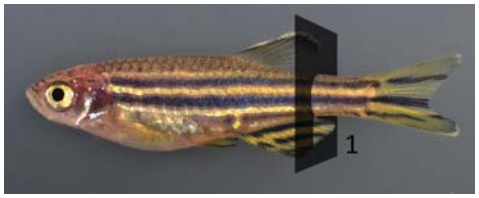

Figure 5.43: B-Scan section.

Figure 5.44 shows the intensity (on a logarithmic scale) of the B-scan and the edge we will use in the next analyses to better evaluate the polarization

Table 5.7: B-Scan: parameters.

Parameter	**Value**
n_{mis}	200
transversal resolution	15 μm
total length	3 mm
time of acquisition	$\sim$ 75 min

figures we present. As we can see, the intensity image is not clear and it doesn't give us much information on the sample in addition to its shape.

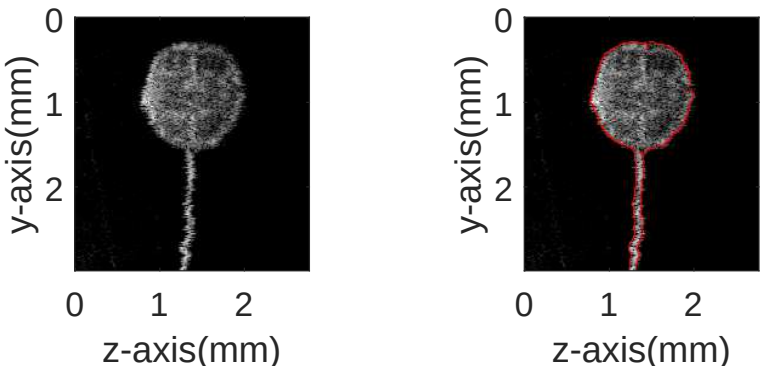

(a) B-Scan image (SOP1). (b) Edge estimation.

Figure 5.44: Horizontal B-Scan.

The following analysis is necessary to show how the muscles within the sample affects the polarization of the light. We report the images of each component of Stokes vector for both the SOPs in Figure 5.45 and Figure 5.46.

We can see how all Stokes vector components changes within the sample due to the birefringence of the muscles and this behaviour is easy to noticed in Figure 5.47, which shows the graphical representation of the Stokes vector on the Poincaré sphere.

The analysis of the behaviour of the polarization within the biological

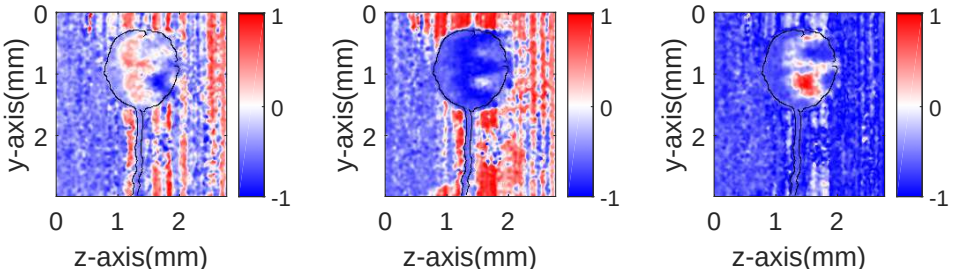

(a) S_1. (b) S_2. (c) S_3.

Figure 5.45: Components of the Normalized Stokes vector for SOP1.

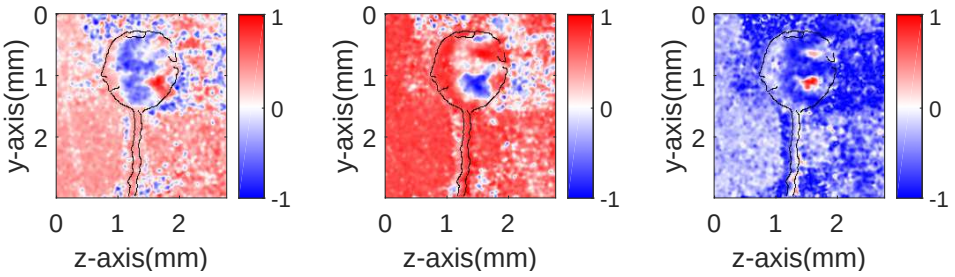

(a) S_1. (b) S_2. (c) S_3.

Figure 5.46: Components of the Normalized Stokes vector for SOP2.

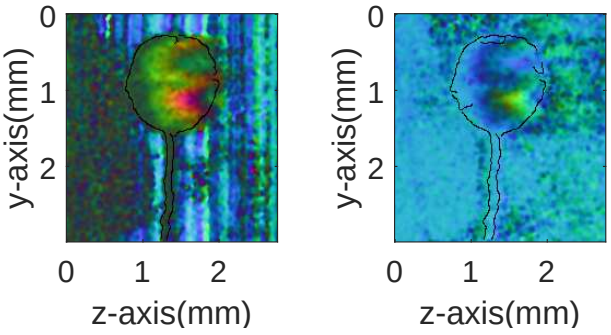

(a) SOP1. (b) SOP2.

Figure 5.47: Graphical representation of the Stokes vector.

sample is reliable due to the high degree of polarization in this area. Figure 5.48 shows the DOP of both SOPs.

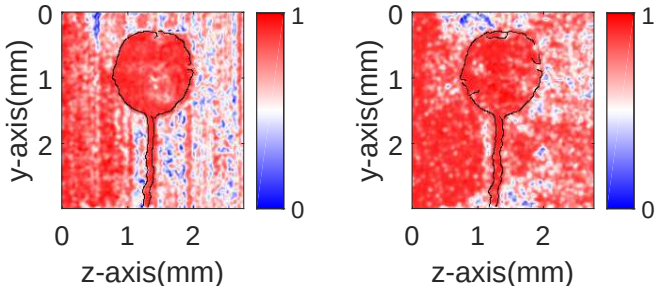

(a) DOP for SOP1. (b) DOP for SOP2.

Figure 5.48: Degree of Polarization of the light for the two SOPs.

These experimental results prove that the muscles of the tail is birefringent as shown in Figure 5.49. Inside the edge the value of birefringence is homogeneous apart from the area in which polarization changes where birefringence is higher than elsewhere, while outside the sample light seems to be only minimally polarized and birefringence information is not reliable there. On the other hand, on the left side light is highly polarized because it still hasn't reached the sample and the information about its birefringence is not correct.

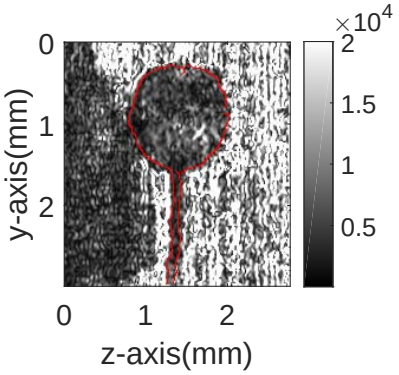

Figure 5.49: Birefringence image of transversal section 1 of the Zebrafish.

Transversal section 2

We also made a transversal scan of the central part of body of the Zebrafish (Figure 5.50). Its parameters are listed in Table 5.8. We chose this

section to compare it with the previous scan and to confirm the lack of birefringence in the central part of the sample that we noticed before.

Figure 5.50: B-Scan section.

Table 5.8: B-Scan: parameters.

Parameter	**Value**
n_{mis}	225
transversal resolution	15 μm
total length	3.375 mm
time of acquisition	$\sim$ 85 min

Figure 5.51 shows the B-scan and the edge as computed by Canny's algorithm. We will use in the next figures to highlight the shape of the sample. As we can see, the intensity image is not complete due to the high absorption of the light in the lower area of the sample probably due to the presence of water in tissues. We identify in the central part of the scan a black area which represents the swim bladder that Prof. Tiso highlighted in previous analyses.

Figure 5.52 and Figure 5.53 show the images of each component of Stokes vector for both the SOPs. We see how the muscles within the upper area of the sample affect the polarization while the lower part of the body doesn't modify the Stokes vector. This behaviour is easy to notice in Figure 5.54, which shows the graphical representation of the Stokes vector on the Poincaré sphere.

The analysis of the behaviour of the polarization within the upper part

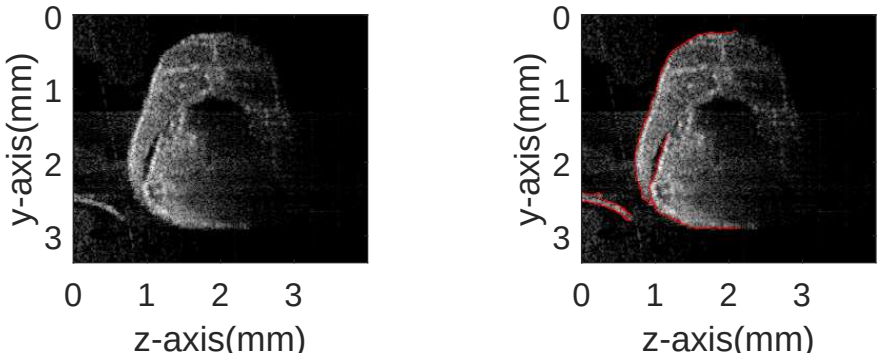

(a) B-Scan image (SOP1). (b) Edge estimation.

Figure 5.51: Horizontal B-Scan.

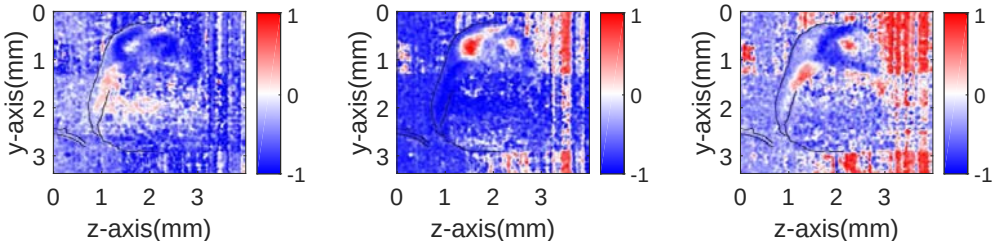

(a) S_1. (b) S_2. (c) S_3.

Figure 5.52: Components of the Normalized Stokes vector for SOP1.

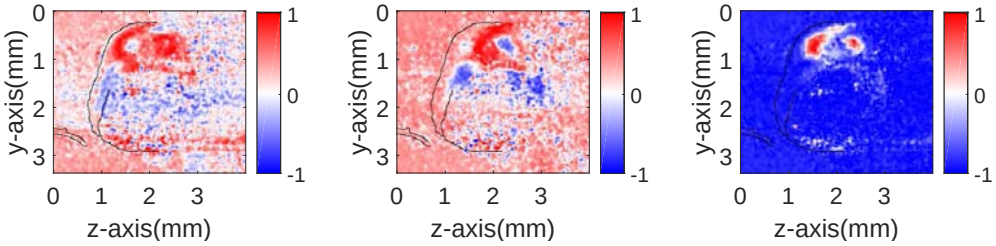

(a) S_1. (b) S_2. (c) S_3.

Figure 5.53: Components of the Normalized Stokes vector for SOP2.

of the biological sample is reliable due to the high degree of polarization as visible in Figure 5.55, which shows the DOP of the SOPs.

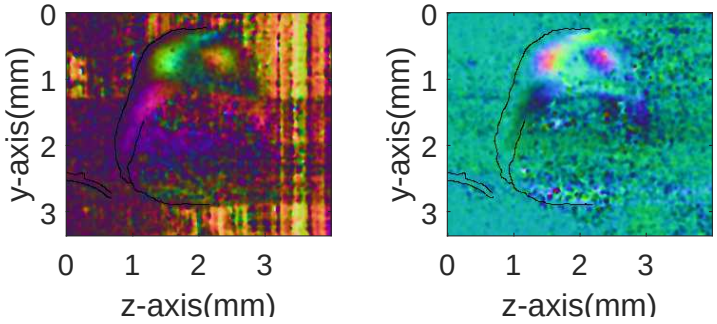

(a) SOP1. (b) SOP2.

Figure 5.54: Graphical representation of the Stokes vector.

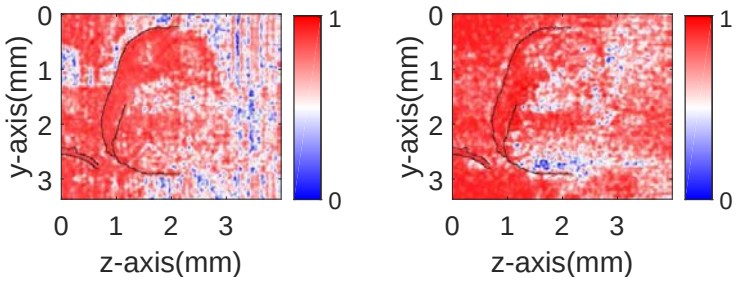

(a) DOP for SOP1. (b) DOP for SOP2.

Figure 5.55: Degree of Polarization of the light for the two SOPs.

These results prove that the muscles in the upper part of the sample is birefringent, which is also visible in Figure 5.56 where we could identify two white spots. On the other hand, the light in the rest of the section exhibits very little polarization and there we cannot have reliable birefringence information.

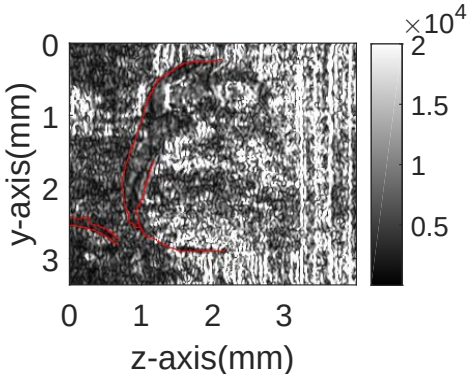

Figure 5.56: Birefringence image of transversal section 2 of the Zebrafish.

Chapter 6

Conclusions

In this thesis we developed an experimental Polarization-Sensitive OCT and we described the physical principles behind the results we found. Firstly we optimized our system in order to obtain high quality images by analysing different concentrations of the suspension we used to suspend the biological sample during the scans. Then we tested both a biological and a non-biological sample, respectively a specimen of Zebrafish and a roll of scotch tape. We showed how these samples are birefringent and in particular we identified a strong correlation between the muscle fibers and the changes in polarization of the light inside the sample, as we expected from the literature. We implemented two different PS-OCT systems: the first one exploits the characteristics of the source (OBR) and its heterodyne measurements of the interference between the two arms of its internal interferometer: that allows us to obtain polarization information about the light beam. We used the second setup to separate the beam into two orthogonal states of polarization in order to study the birefringence properties of the sample.

The performance we obtained from these two systems can be improved significantly with the use of a different source. In fact, the instrumentation we used is not optimized for this application: the OBR forces us to use an optical range where the absorption of light is high in biological tissues. OCT systems, instead, usually use tunable lasers with operating wavelengths around 1300 nm and separate receivers that offer better performance and the possibility to obtain real time images.

Future developments should exploit the non-linear behaviour of the absorption of light with different concentrations of agarose. The use of galvanometric mirrors in place of the piezoelectric translator can increase the robustness and the reliability of the system, by removing the possible interference caused by the movement of the sample. The use of a tunable laser with a dedicated detector would yield real time images with the possibility to create C-Scans, 3D images of the samples. Also a measurement of the complete birefringence vector of the tissues should be made, so as to determine not only the birefringence strength as in this work, but also its orientation.

Bibliography

[1] J. Fujimoto, C. Pitris, S. Boppart, and M. Brezinski, "Optical coherence tomography: An emerging technology for biomedical imaging and optical biopsy," *Neoplasia*, 2000.

[2] B. Elmaanaoui, B. Wang, J. Dwelle, A. McElroy, S. Liu, H. Rylander III, and T. Milner, "Birefringence measurement of the retinal nerve fiber layer by swept source polarization sensitive optical coherence tomography," *Optics Express*, 2011.

[3] Z. Wang, H.-C. Lee, O. Ahsen, B. Lee, W. Choi, B. Potsaid, J. Liu, V. Jayaraman, A. Cable, M. Kraus, K. Liang, J. Hornegger, and J. Fujimoto, "Depth-encoded all-fiber swept source polarization sensitive oct," *Biomedical Optics Express*, 2014.

[4] B. Park, M. Pierce, B. Cense, and J. De Boer, "Jones matrix analysis for a polarization-sensitive optical coherence tomography system using fiber-optic components," *Optics Letters*, 2004.

[5] M. Yamanari, S. Makita, T. Yatagai, and t. . Yasuno, Y."

[6] B. Baumann, W. Choi, B. Potsaid, D. Huang, J. Duker, and t. . Fujimoto, J.G."

[7] Y. Lim, Y.-J. Hong, L. Duan, M. Yamanari, and t. . Yasuno, Y."

[8] M. Brezinski, *Optical Coherence Tomography: Principles and Applications*. Elsevier Inc., 2006.

[9] M. Bernardello and L. Palmieri, "Sviluppo sperimentale di un tomografo a coerenza ottica," Master's thesis, Univerity of Padova, 2013.

[10] P. Rossignoli and L. Palmieri, "Ps-oct," Master's thesis, Univerity of Padova, 2015.

[11] Wordpress, "Putting the laser shop on line." `https://laseroflove.files.wordpress.com/2010/03/0330270307003.png`.

[12] A. Javier, "Laser and gaussian beam propagation and transformation," *Encyclopedia of Optical Engineering*, 2003.

[13] W. Wieser, G. Palte, C. M. Eigenwillig, B. R. Biedermann, T. Pfeiffer, and R. Huber, "Chromatic polarization effects of swept waveforms in fdml lasers and fiber spools," *Optics Express*, 2012.

[14] M. F. Kraus, B. Potsaid, M. A. Mayer, R. Bock, B. Baumann, J. J. Liu, J. Hornegger, and J. G. Fujimoto, "Motion correction in optical coherence tomography volumes on a per a-scan basis using orthogonal scan patterns," *Biomedical Optics Express*, 2012.

[15] K. at English Wikipedia, "Absorption spectrum of liquid water." `https://commons.wikimedia.org/wiki/File:Absorption_spectrum_of_liquid_water.png#/media/File:Absorption_spectrum_of_liquid_water.png`.

[16] P. C. W. adn Tony H. Ko, J. G. Fujimoto, F. X. Kaertner, and U. Morgner, "Ultrahigh-resolution optical coherence tomography with a diode-pumped broadband cr^{3+}:licaf laser," *Optics Express*, 2004.

[17] E. J. Galvez, "Gaussian beams," tech. rep., Department of Physics and Astronomy, Colgate University, 2009.

[18] P. H. Tomlins and R. K. Wang, "Theory, developments and applications of optical coherence tomography," *Journal of Physics D: Applied Physics*, 2005.

[19] D. T. Miller, O. P. Kocaoglu, Q. Wang, and S. Lee, "Adaptive optics and the eye (super resolution oct)," *Eye*, 2011.

[20] L. Palmieri, "Distributed polarimetric measurements for optical fiber sensing," *Optical Fiber Technology*, 2013.

[21] K. Kanatani, "Analysis of 3-d rotation fitting," *IEEE Transactions on Pattern Analysis and Machine Intelligence*, 1994.

[22] L. Nelson, R. Jopson, and H. Kogelnik, "Measurement of second-order polarization-mode dispersion vectors in optical fibers," in *IEEE Photonics Technology Letters*, 1999.

[23] "Optical Backscatter Reflectometer User Guide". Luna Technologies Inc., 2006.

[24] T. Inc., "Thorlabs website." `https://www.thorlabs.com`.